Constrained Large-Eddy Simulation of Compressible Flow Past a Circular Cylinder

Renkai Hong[1], Zhenhua Xia[1], Yipeng Shi[1,2,*], Zuoli Xiao[1,2,*] and Shiyi Chen[1,2,*]

[1] *State Key Laboratory for Turbulence and Complex Systems, College of Engineering, Peking University, Beijing 100871, P.R. China.*
[2] *Center for Applied Physics and Technology, College of Engineering, Peking University, Beijing 100871, P.R. China*

Abstract. Compressible flow past a circular cylinder at an inflow Reynolds number of 2×10^5 is numerically investigated by using a constrained large-eddy simulation (CLES) technique. Numerical simulation with adiabatic wall boundary condition and at a free-stream Mach number of 0.75 is conducted to validate and verify the performance of the present CLES method in predicting separated flows. Some typical and characteristic physical quantities, such as the drag coefficient, the root-mean-square lift fluctuations, the Strouhal number, the pressure and skin friction distributions around the cylinder, *etc.* are calculated and compared with previously reported experimental data, finer-grid large-eddy simulation (LES) data and those obtained in the present LES and detached-eddy simulation (DES) on coarse grids. It turns out that CLES is superior to DES in predicting such separated flow and that CLES can mimic the intricate shock wave dynamics quite well. Then, the effects of Mach number on the flow patterns and parameters such as the pressure, skin friction and drag coefficients, and the cylinder surface temperature are studied, with Mach number varying from 0.1 to 0.95. Non-monotonic behaviors of the pressure and skin friction distributions are observed with increasing Mach number and the minimum mean separation angle occurs at a subcritical Mach number of between 0.3 and 0.5. Additionally, the wall temperature effects on the thermodynamic and aerodynamic quantities are explored in a series of simulations using isothermal wall boundary conditions at three different wall temperatures. It is found that the flow separates earlier from the cylinder surface with a longer recirculation length in the wake and a higher pressure coefficient at the rear stagnation point for higher wall temperature. Moreover, the influences of different thermal wall boundary conditions on the flow field are gradually magnified from the front stagnation point to the rear stagnation point. It is inferred that the CLES approach in its current version is

Corresponding author. Email addresses: `hongrenkai@163.com` (R. Hong), `xiazh@pku.edu.cn` (Z. Xia), `syp@mech.pku.edu.cn` (Y. Shi), `z.xiao@pku.edu.cn` (Z. Xiao), `syc@pku.edu.cn` (S. Chen)

a useful and effective tool for simulating wall-bounded compressible turbulent flows with massive separations.

1 Introduction

Flow around a circular cylinder is of great importance, either in practical engineering problems such as wind past a cooling tower, lateral flow past an aircraft body, or in fundamental research problems. As the cylinder surface is smooth and curved, a sensitive boundary layer forms and will separate from the surface if the inflow Reynolds number is high enough. The transition of flow to turbulence may take place either in the boundary layer (*i.e.*, turbulent separation) or in the separated shear layer (*i.e.*, laminar separation). The interactions among the three shear layers, say, the boundary layer, the separated free shear layer and the wake, result in complex physical phenomena in incompressible case [1]. The first experimental study on this problem was carried out by Bénard [2] at the beginning of the twentieth century. Then, von Kármán [3] and Thom [4] investigated the same problem theoretically and numerically, respectively. These seminal works have sparked increasing interests and challenges in understanding the intricate dynamics of flow past a circular cylinder. The readers are referred to the review articles [5–8] and textbooks [9,10] for details. In fact, the geometrical simplicity and the availability of numerical and experimental data of flow past a circular cylinder have suggested that it be a benchmark model to validate a numerical solver or a turbulence model both in incompressible cases [11–18] and in compressible cases [19–21].

In compressible flow past a circular cylinder, especially at transonic inflow conditions, the problem becomes more complicated due to the three mutually coupled fundamental processes (*i.e.*, compressing, shearing, and thermal). Related topics include compressible boundary layer instability, shock wave/boundary layer interactions, shock wave/wake interactions, *etc*. Macha systematically examined the pressure distributions and the drag coefficients around a circular cylinder in a wind tunnel at Reynolds and Mach numbers from 0.1×10^6 to 1.0×10^6 and from 0.6 to 1.2, respectively [22]. As Mach number increases, it is shown that the pressure drag keeps increasing before Mach 0.7, remains constant or decreases slightly from Mach 0.7 to Mach 0.9, increases dramatically near Mach 1.0 and decreases monotonically when Mach number is larger than unit. It is argued that the leveling-off of the drag variation prior to the major drag crisis near Mach 1.0 be attributed to the compressibility effects. Murthy and Rose [23] also conducted a series of wind tunnel experiments on air flow past a circular cylinder with Mach and Reynolds numbers varying from 0.25 to 1.2 and from 0.03×10^6 to 0.5×10^6, respectively. The transonic drag rise phenomenon was also observed. Meanwhile, it is found that detectable

periodic shedding ceases at about Mach 0.9. Rodriguez [24] investigated the subsonic and transonic flows around a circular cylinder at Reynolds numbers of about 10^5. As is shown by his experimental results, there exist strong coupling between the flow over the cylinder and the vortex street in the near wake. Various coupling regimes are classified and instantaneous pressure distributions are obtained and analyzed at different times in a vortex street period.

Compressible flow around a circular cylinder has also been studied via numerical simulations. Miserda and Leal [25] investigated the unsteady forces and the flow structures generated in transonic flow past a circular cylinder through solving either the unsteady Reynolds-averaged or spatially-filtered compressible two-dimensional (2D) Navier-Stokes equations with SST-DES model using a finite-volume method. The inflow Mach and Reynolds numbers are 0.8 and 5×10^5, respectively. It is shown that the dominant frequency of the unsteady lift coefficient is closely related to the vortex-shedding frequency. The complex interactions between the shearing processes and the compressing process were also discussed. Xu *et al.* [26] evaluated the effects of Mach number on typical flow phenomena for transonic flows past a circular cylinder, including shock wave/turbulent boundary layer interactions, the formation of local supersonic zones and shocklets in the wake and the evolution of the turbulent shear layer. It is suggested that there be a critical Mach number of about 0.9, above which the flow is quasi-steady and the vortex shedding is suppressed. Recently, Xu *et al.* [21] conducted a numerical investigation of the physical mechanisms concerning the passive control of compressible flow past a wavy cylinder by using large-eddy simulation. It is shown that the wavy surface of the cylinder plays an effective role in eliminating or suppressing the shock waves and shocklets observed in flow around a circular cylinder.

The simplest approach to numerical exploration of turbulent flows is the direct numerical simulation (DNS), which is free of modeling assumptions. However, DNS has been limited to simple geometries at low or moderate Reynolds numbers due to the intolerable computational cost and its application to practical engineering problems is still far from feasible in the near future. Reynolds-averaged Navier-Stokes (RANS) simulation technique has been widely used in commercial software for engineering flows with low requirement for computing grids, but its application to unsteady and separated flows patterns remains questionable and unsatisfactory due to the lack of generality of turbulence models. Large-eddy simulation (LES), whose computational cost is between DNS and RANS approaches, can predict three-dimensional (3D) and unsteady flow fields by solving the spatially-filtered Navier-Stokes equations with the subgrid-scale (SGS) models being more "universal" than those for RANS. Nevertheless, LES still requires fairly fine grids when used to solve the wall-bounded turbulent flows of engineering interest. Such a situation has considerably stimulated the development of the hybrid RANS/LES methods, among which is the commonly employed detached-eddy simulations (DES) technique [36]. In this type of approaches, the computation domain is usually divided into two regions along the wall-normal direction. The RANS equations are solved in the near-wall region, while the LES equations are integrated in the outer region. The hybrid

RANS/LES method takes the advantages both from the RANS solutions in the near wall region and from the LES solutions in the outer region, and has contributed a lot to the simulation for engineering flows, especially for the complex flows with massive separations. Yet with the inherent advantages, the hybrid RANS/LES methods have problematic drawbacks. For example, DES encounters the well-known log-layer mismatch (LLM) defect in predicting a simple turbulent channel flow [27]. As claimed by Fröhlich and von Terzi [28], "the unphysical deviations in the mean flow profiles appearing at the inner-outer layer interface may cast doubts on the quality of predictions made with such approaches, in particular for applications where the near-wall flow structures play a significant role." Readers are suggested to check the review articles by Fröhlich and von Terzi [28] and Spalart [29] for more detailed descriptions and discussions on the hybrid RANS/LES methods.

In order for the LES to be feasible to numerically predict wall-bounded turbulent flows, Chen *et al.* [30] proposed a so-called Reynolds-stress constrained large-eddy simulation (CLES) methodology, in which the whole flow domain is simulated through solving the LES equations with the modeled mean SGS stress constrained by a Reynolds stress balance condition in the near wall region. Such a Reynolds stress constraint can ensure an accurate mean velocity distribution near the wall, which cannot be achieved in traditional LES if the mesh is not fine enough. In the Reynolds stress balance relation, the total Reynolds stress is modeled based on the resolved velocity field without solving the RANS equations. The Reynolds stress CLES method was tested and validated in simulation of incompressible turbulent channel flow and incompressible flow past a circular cylinder. For turbulent channel flow, the CLES method can predict the mean velocity profile very well without the LLM phenomena, and can calculate the skin friction more accurately as compared with the DES method and the traditional LES method using dynamic Smagorinsky model. It is the first time for pure LES method to be used to simulate flow past a circular cylinder at a Reynolds number based on the diameter of cylinder up to 3×10^6 and the results are also encouraging when compared with available experimental data.

Jiang *et al.* [31] extended the CLES method for incompressible turbulent flows to a new version for wall-bounded compressible turbulent flows. In the compressible CLES approach, a Reynolds heat flux balance condition is introduced for the modeled mean SGS heat flux vector in addition to the Reynolds stress constraint for the SGS stress tensor. The new CLES method are tested and verified in simulations of compressible turbulent channel flow and the results are well compared with those obtained from traditional LES, DES and DNS. The corresponding paper is under consideration for publication in other journal. Chen *et al.* [32] carried out a pure LES of flow past a commercial plane at 14° angle of attack by using the compressible CLES technique. It is shown that CLES can predict more fruitful and much smaller vortex structures than DES and RANS methods.

In this paper, compressible flow past a circular cylinder is investigated utilizing the compressible CLES approach proposed by Jiang *et al.* [31] at Reynolds number $Re = 2 \times 10^5$ based on the diameter of cylinder. The purpose of the present paper is threefold. First,

we demonstrate the validity of the new CLES method in predicting wall-bounded compressible flows with massive separations. Compressible flow around a circular cylinder is simulated at a free-stream Mach number $Ma = 0.75$ with adiabatic wall boundary condition. The statistical results are compared with those obtained from the experimental measurements [22–24], the previously reported LES on a much finer mesh [21] and the present LES and DES on the same coarse-resolution grids. Second, we explore the Mach number effects on the flow patterns, the drag coefficient, the pressure distribution, *etc*. Finally, we provide some insight into the influences of wall temperature on the flow phenomena by using isothermal wall boundary condition.

   The remaining contents of this paper are as follows. The governing equations are presented in Section 2. Section 3 concentrates on the introduction of the CLES and DES formulations as well as the numerical methods. Section 4 focuses on the validation of the compressible CLES method. The shock wave/shock wave and shock wave/turbulence interactions are studied using the compressible CLES approach in Section 5. Section 6 and Section 7 contributes to the studies of Mach number and wall temperature effects, respectively. Finally, conclusions and discussions are made in Section 8.

2   Governing equations

The governing equations for LES of compressible turbulent flows can be obtained by applying a low-pass filter to the mass, momentum and energy conservation equations. If one defines characteristic parameters using the diameter of cylinder D, the free-stream velocity U_∞, density ρ_∞, temperature T_∞, dynamic viscosity μ_∞ and thermal conductivity κ_∞, the filtered conservation equations are written as the following dimensionless form [31]

$$\frac{\partial \bar{\rho}}{\partial t} + \frac{\partial (\bar{\rho}\widetilde{u}_i)}{\partial x_i} = 0, \tag{2.1}$$

$$\frac{\partial (\bar{\rho}\widetilde{u}_i)}{\partial t} + \frac{\partial (\bar{\rho}\widetilde{u}_i\widetilde{u}_j + \bar{p}\delta_{ij})}{\partial x_j} = \frac{1}{Re}\frac{\partial \widetilde{\sigma}_{ij}}{\partial x_j} + \frac{\partial \tau_{ij}^{LES}}{\partial x_j}, \tag{2.2}$$

$$\frac{\partial (\bar{\rho}\widetilde{e})}{\partial t} + \frac{\partial [\widetilde{u}_i(\bar{\rho}\widetilde{e} + \bar{p})]}{\partial x_i} = \frac{\partial \widetilde{q}_i}{\partial x_i} + \frac{1}{Re}\frac{\partial (\widetilde{\sigma}_{ij}\widetilde{u}_j)}{\partial x_i} + \frac{\partial q_i^{LES}}{\partial x_i} + \frac{\partial J_i^{LES}}{\partial x_i}, \tag{2.3}$$

which are accompanied with the thermodynamical equation of state

$$\bar{p} = \frac{\bar{\rho}\widetilde{T}}{\gamma M_\infty^2}. \tag{2.4}$$

Here, $\overline{f}$ represents a spatially-filtered field, and $\widetilde{f} = \frac{\overline{\rho f}}{\bar{\rho}}$ denotes a Favre-filtered field [33]. $\bar{\rho}$ is the density, $\widetilde{u}_i$ is the velocity vector, $\overline{p}$ is the pressure, $\widetilde{T}$ is the temperature, $\widetilde{e} = C_v\widetilde{T} + \frac{1}{2}\widetilde{u}_i\widetilde{u}_i$ is the total energy per unit mass, $C_v = 1/\gamma(\gamma - 1)M_\infty^2$ is the specific heat at constant

volume, γ is the ratio of specific heats, $C_p = \gamma C_v$ is the specific heat at constant pressure, $M_\infty = U_\infty / \sqrt{\gamma R T_\infty}$ is the Mach number, R is the specific gas constant, $Re = \rho_\infty U_\infty D / \mu_\infty$ is the Reynolds number,

$$\widetilde{\sigma}_{ij} = \mu(\widetilde{T}) \left(\frac{\partial \widetilde{u}_i}{\partial x_j} + \frac{\partial \widetilde{u}_j}{\partial x_i} - \frac{2}{3} \frac{\partial \widetilde{u}_k}{\partial x_k} \delta_{ij} \right) \tag{2.5}$$

and

$$\widetilde{q}_i = -\frac{C_p \mu(\widetilde{T})}{RePr} \frac{\partial \widetilde{T}}{\partial x_i} \tag{2.6}$$

are, respectively, the viscous stress tensor and the heat flux vector, in which $P_r = C_p \mu_\infty U_\infty^2 / \kappa_\infty T_\infty = 0.7$ is the molecular Prandtl number and μ is the dimensionless viscosity given by Sutherland's law

$$\mu = \frac{\widetilde{T}^{3/2}(1+S)}{\widetilde{T}+S}, \tag{2.7}$$

with $S = 110.3K/T_\infty$.

There exist three unclosed terms in Eq. (2.2) and Eq. (2.3), namely, the SGS stress tensor

$$\tau_{ij}^{LES} = -\bar{\rho}(\widetilde{u_i u_j} - \widetilde{u}_i \widetilde{u}_j), \tag{2.8}$$

the SGS heat flux vector

$$q_i^{LES} = -\bar{\rho} C_p (\widetilde{Tu_i} - \widetilde{T}\widetilde{u}_i), \tag{2.9}$$

and the triple velocity correlation term

$$J_i^{LES} = -\frac{1}{2}\bar{\rho}(\widetilde{u_j u_j u_i} - \widetilde{u_j u_j}\widetilde{u}_i). \tag{2.10}$$

As suggested in previous studies [34,35], J_i^{LES} can be approximated using the SGS stress tensor in the form

$$J_i^{LES} = \tau_{ij}^{LES}\widetilde{u}_j. \tag{2.11}$$

Therefore, in the present study, closure models for τ_{ij}^{LES} and q_i^{LES} need to be supplemented based on the resolved fields.

3   Simulation and numerical methods

3.1   The DES method

The DES method has attracted increasing attention in a sense of both turbulence modeling research and engineering application [28, 29] since it was originally proposed by Spalart *et al.* in 1997 [36]. The aim of the DES method is to numerically predict separated

flows at unlimited Reynolds number and affordable computational cost. In DES, a unified system of the control equations (see, *e.g.*, Eqs. (2.1)-(2.4)) is solved by incorporating prescribed RANS models in the near-wall region and SGS models in the rest region, respectively. In principle, any available RANS model can be modified and adopted in the DES formulation. In this work, the most commonly used version of DES method based on the one equation Spalart-Allmaras (S-A) model [37] is implemented in order to evaluate the performance of the CLES method. The RANS and SGS models for stress and heat flux take the same form as follows

$$\tau_{ij}^{MOD} = \mu_t \left(2\hat{S}_{ij} - \frac{2}{3}\frac{\partial \hat{u}_k}{\partial x_k}\delta_{ij} \right), \tag{3.1}$$

and

$$q_i^{MOD} = -\frac{C_p \mu_t}{Pr_t}\frac{\partial \hat{T}}{\partial x_i}, \tag{3.2}$$

with a *hat* denoting ensemble averaging in RANS model or spatial filtering in SGS model. The turbulent (or eddy) viscosity μ_t is determined by an intermediate viscosity $\mathring{v}$, which can be obtained by solving the following equation as suggested by Edwards and Chandra [38]

$$\frac{D\hat{\rho}\mathring{v}}{Dt} = c_{b1}\mathring{S}\hat{\rho}\mathring{v} + \frac{1}{\sigma}\left(\frac{\partial}{\partial x_j}(\mu + \hat{\rho}\mathring{v})\frac{\partial \mathring{v}}{\partial x_j} + c_{b2}\frac{\partial \mathring{v}}{\partial x_j}\frac{\partial \hat{\rho}\mathring{v}}{\partial x_j} \right) - \hat{\rho}c_{w1}f_w\left(\frac{\mathring{v}}{\mathring{d}} \right)^2. \tag{3.3}$$

Thus, μ_t is related to $\mathring{v}$ through the following relation

$$\mu_t = \hat{\rho}\mathring{v}f_{v1}, \quad f_{v1} = \frac{\lambda^3}{\lambda^3 + c_{v1}^3}, \quad \lambda \equiv \frac{\mathring{v}}{v}.$$

Given the vorticity magnitude

$$\hat{S} = \left[\left(\frac{\partial \hat{u}_i}{\partial x_j} + \frac{\partial \hat{u}_j}{\partial x_i} \right)\frac{\partial \hat{u}_i}{\partial x_j} - \frac{2}{3}\left(\frac{\partial \hat{u}_k}{\partial x_k} \right)^2 \right]^{1/2},$$

the modified vorticity magnitude $\mathring{S}$ in Eq. (3.3) reads

$$\mathring{S} = \hat{S}\left(\frac{1}{\lambda} + f_{v1} \right).$$

The parameters f_{v2} and f_w are given by

$$f_{v2} = 1 - \frac{1}{1 + \lambda f_{v1}}, \quad f_w = g\left[\frac{1 + c_{w3}^6}{g^6 + c_{w3}^6} \right]^{1/6}$$

with

$$g = r + c_{w2}(r^6 - r), \quad r = \tanh\left[\frac{\mathring{v}}{(k\mathring{d})^2\mathring{S}} \right]/[\tanh(1.0)].$$

The length scale $\mathring{d}$ is defined as

$$\mathring{d} \equiv \min(d, C_{DES}\Delta),$$

with d being the distance to the nearest wall and $\Delta \equiv \max(\Delta x, \Delta y, \Delta z)$ the maximum local mesh size. The DES method solves the RANS equations when $\mathring{d}$ is equal to d, and solves the LES equations when $\mathring{d}$ is equal to $C_{DES}\Delta$. The empirical constants in Eq. (3.3) are listed below

$$c_{b1} = 0.1355, \quad c_{b2} = 0.622, \quad c_{w2} = 0.3, \quad c_{v1} = 7.1, \quad \sigma = \frac{2}{3}, \quad c_{w1} = \frac{c_{b1}}{k^2} + \frac{1 + c_{b2}}{\sigma}, \quad c_{w3} = 2.$$

3.2 The CLES method

Chen *et al.* [30] argued that LES of wall-bounded turbulent flow is feasible on well-designed coarse-resolution grids as long as the mean SGS stress in the near-wall region is constrained by a Reynolds stress balance condition. The LES using such an SGS model is referred to as Reynolds stress constrained large-eddy simulation (RS-CLES) and has been implemented and verified in simulating the incompressible wall-bounded turbulent flows with and without separations.

Recently, Jiang *et al.* [31] extended the RS-CLES methodology to a new formulation aiming at the simulation of compressible turbulent flows with wall boundaries. In the compressible CLES method, both the SGS stress and the SGS heat flux (*i.e.*, τ_{ij}^{LES} and q_i^{LES} shown in Eq. (2.2) and Eq. (2.3)) are decomposed into a mean part and a fluctuation part in the near-wall region of the flow domain, *i.e.*,

$$\tau_{ij}^{LES} = \langle \tau_{ij}^{LES} \rangle + \tau_{ij}^{LES\prime} \tag{3.4}$$

and

$$q_i^{LES} = \langle q_i^{LES} \rangle + q_i^{LES\prime}. \tag{3.5}$$

The mean SGS stress and heat flux are given by

$$\langle \tau_{ij}^{LES} \rangle = \tau_{ij}^{RANS} + \langle \overline{\rho} \rangle (|\tilde{u}_i \tilde{u}_j| - |\tilde{u}_i||\tilde{u}_j|), \tag{3.6}$$

and

$$\langle q_i^{LES} \rangle = q_i^{RANS} + \langle \bar{\rho} \rangle C_p (|\tilde{u}_i \tilde{T}| - |\tilde{u}_i||\tilde{T}|), \tag{3.7}$$

respectively. Here, $\langle \cdot \rangle$ denotes a ensemble average, and $|\cdot|$ represents a Favre average. The total Reynolds stress τ_{ij}^{RANS} and the total Reynolds heat flux q_i^{RANS} shall be prescribed by the S-A models discussed in Section 3.1 (see Eq. (3.1) and Eq. (3.2)) based on the resolved fields. The SGS stress and heat flux fluctuations are given according to the

compressible Smagorinsky models [35] in the following form

$$\tau_{ij}^{LES\prime} = 2C_s \left[\bar{\rho}\Delta^2 |\widetilde{S}| \left(\widetilde{S}_{ij} - \frac{1}{3}\widetilde{S}_{kk}\delta_{ij} \right) - \left\langle \bar{\rho}\Delta^2 |\widetilde{S}| \left(\widetilde{S}_{ij} - \frac{1}{3}\widetilde{S}_{kk}\delta_{ij} \right) \right\rangle \right]$$
$$- \frac{2}{3}C_I \left[\bar{\rho}\Delta^2 |\widetilde{S}|^2 - \left\langle \bar{\rho}\Delta^2 |\widetilde{S}|^2 \right\rangle \right]\delta_{ij}, \tag{3.8}$$

$$q_i^{LES\prime} = \frac{C_s}{Pr_T} \left(\Delta^2 \bar{\rho}C_p |\widetilde{S}|\frac{\partial \widetilde{T}}{\partial x_i} - \left\langle \Delta^2 \bar{\rho}C_p |\widetilde{S}|\frac{\partial \widetilde{T}}{\partial x_i} \right\rangle \right). \tag{3.9}$$

Here, C_s and C_I are the Smagorinsky constants, Pr_T is the SGS Prandtl number. In this paper, C_I is taken to be zero as suggested in previous studies [39–41]. C_s and Pr_T can be prescribed *a priori* or be calculated instantaneously by a dynamic procedure. For details of the derivation of the CLES models, readers are referred to the paper by Chen *et al.* [30] for incompressible turbulence and the paper by Jiang *et al.* [31] for compressible turbulence. In the rest region of the flow domain, the traditional Smagorinsky models for the SGS stress and heat flux [35] are employed. The compressible CLES method has been tested and validated in the simulation of compressible turbulent channel flow at various Reynolds and Mach numbers [31].

3.3 Numerical method

In order to simulate compressible flows past a circular cylinder, the governing equations (*e.g.*, Eqs. (2.1)-(2.4)) are numerically integrated based on a self-developed finite volume solver on non-staggered grids in generalized curvilinear coordinates. The nonlinear terms are discretized via an advection upstream splitting method (AUSM$^+$) [42–44]. The van Leer's minmod limiter [45] is utilized at the interface to stabilize the computation of the flux. The viscous terms are discretized by using traditional second-order central difference scheme. The temporal advancement of the equations is achieved using an implicit LU-SGS method with sub-iterations to improve the accuracy. As shown in Fig. 1, O-type grids are generated for the simulation domain, which is bounded by 25D
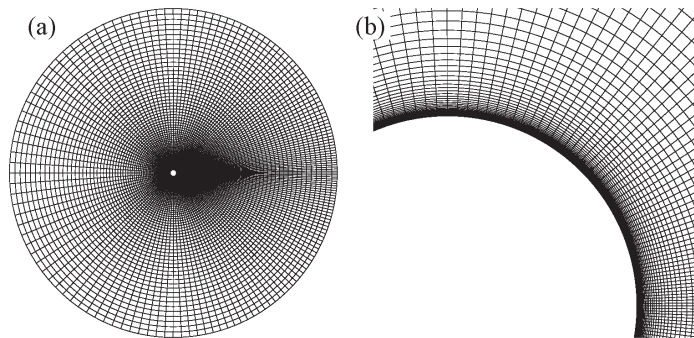

Figure 1: (a) Cross-sectional grids of the computation domain and (b) zoom view of the near-wall grids.

Table 1: Computational parameters and statistical results for the present numerical simulations using LES, DES and CLES at Mach number $M_\infty = 0.75$ and Reynolds number $Re = 2 \times 10^5$ in comparison with previously reported numerical data (fine-resolution LES by Xu *et al.* [21] at $M_\infty = 0.75$ and $Re = 2 \times 10^5$) and experimental data (EXP-1: by Rodriguez [24] at $M_\infty = 0.75$ and $Re = 1.7 \times 10^5 - 3.4 \times 10^5$; EXP-2: by Murthy & Rose [23] at $M_\infty = 0.8$ and $Re = 1.66 \times 10^5$: EXP-3: by Macha [22] at $M_\infty = 0.8$ and $Re = 10^5 - 10^6$).

Case	Grid	$U_\infty \triangle t/D$	C_D	C_{Lrms}	St	θ_{sep}
LES	$128 \times 160 \times 40$	0.02	1.598	0.282	0.187	88.9°
DES	$128 \times 160 \times 40$	0.02	1.616	0.315	0.187	87.5°
CLES	$128 \times 160 \times 40$	0.02	1.571	0.287	0.188	86.1°
LES by Xu *et al.* [21]	$257 \times 257 \times 61$	0.006	1.572	0.250	0.180	
EXP-1			1.618	0.253	0.2	
EXP-2			1.5		0.18	
EXP-3			1.5-1.6			

in the radial direction of the cross section, and by πD in the spanwise direction. There are 128×160 nonuniform control volumes in the cross sectional plane with enough grid points near the cylinder surface and within the wake regions. The first offwall grid height is about $2 \times 10^{-5} D$, which is less than unity in wall units as claimed for effective LES of near-wall flow field. There are 40 uniformly distributed control volumes in the spanwise direction. The constant free-stream quantities, such as U_∞, T_∞, *etc.*, are prescribed at the inlet of the flow and the boundary conditions at the outlet of the flow are determined by the local one-dimensional Riemann-invariants. Non-slip and adiabatic (or isothermal) wall boundary conditions are employed for kinetic and thermodynamic quantities, respectively, on the cylinder surface. Periodic boundary conditions are used in spanwise direction. All the calculations in this study are carried out on the same O-type grid (see Fig. 1). The computational parameters are summarized in Table 1.

4 Validation of the CLES method

In this section, the CLES method for compressible turbulent flows is tested and validated by simulating of compressible flow past a circular cylinder with adiabatic wall boundary condition and at free-stream Mach and Reynolds numbers of 0.75 and 2×10^5, respectively. LES based on traditional eddy-viscosity and eddy-diffusivity models [35] and DES are also conducted using the same solver introduced in Section 3.3. To evaluate the performance of the CLES method in predicting compressible flows with separations and shock waves, the calculated results are compared with the LES results on fine-resolution grids by Xu *et al.* [21] and the experimental data at similar Mach and Reynolds numbers by Rodriguez [24], Murthy & Rose [23], and Macha [22]. Some important statistical quantities are listed in Table 1.

Shown in Fig. 2 are the time-dependent lift (dashed lines) and drag (solid lines) coefficients from LES (panel (a)), DES (panel (b)), and CLES (panel (c)). The time-averaged
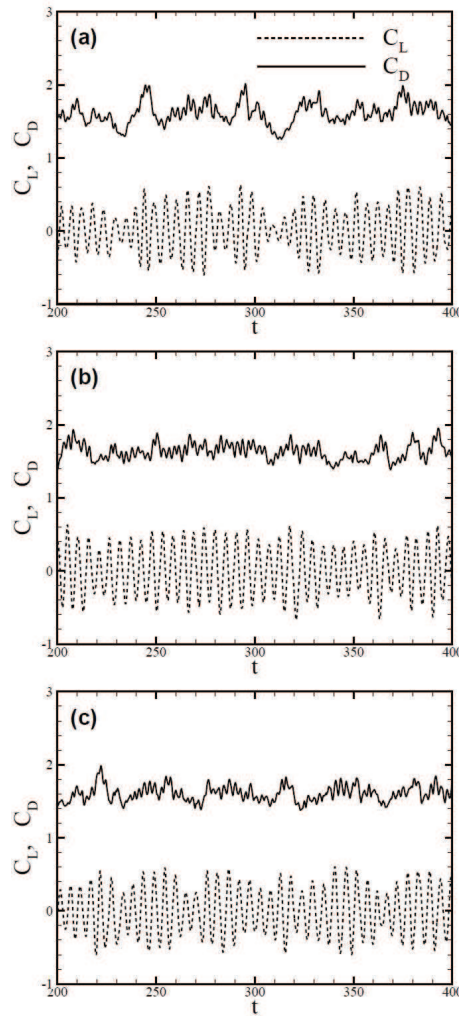
Figure 2: Time-dependent lift (dashed lines) and (solid lines) drag coefficients on the circular cylinder from (a) LES, (b) DES, and (c) CLES.

drag coefficient (C_D) and the root-mean-square (rms) value of lift fluctuations (C_{Lrms}) are listed in Table 1. It can seen that all the time-averaged drag coefficients calculated in the present simulations fall in the range of experimental data, about 1.5 to 1.618, while the value predicted by CLES is nearly identical to that calculated in LES on fine-resolution grids by Xu *et al.* [21]. However, the values of C_{Lrms} obtained in the present calculations are larger than those obtained in experiment by Rodriguez [24] and LES by Xu *et al.* [21]. The present LES and CLES overestimate C_{Lrms} at a 12% level as compared with experimental measurement, while the value given in DES is 24.5% larger than the experimental value. As is well known, the fluctuating force (*e.g.*, the fluctuating lift) on a circular cylinder is highly associated with the vortex shedding phenomenon in the wake, which is
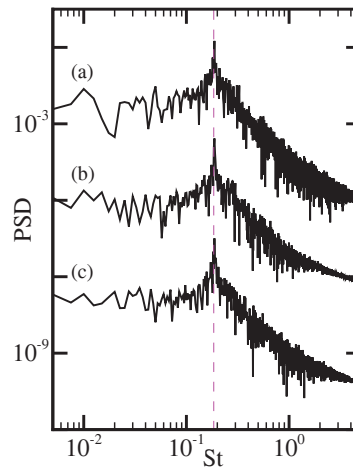
Figure 3: Power spectral density (PSD) of the time-dependent lift coefficient from the present calculations: (a) LES, (b) DES, and (c) CLES.

usually identified by the power spectral density (PSD) of the time-dependent lift coefficient [46, 47]. Fig. 3 shows the PSD of the time-dependant lift coefficient for the present calculations in terms of Strouhal number, which is defined as $St = fD/U_\infty$ with f being the vortex shedding frequency. The primary frequency corresponds to the peak of the PSD. As can be seen in Table 1, the primary frequencies for LES, DES and CLES are comparable to each other, *i.e.*, 0.187, 0.187 and 0.188, respectively, and are consistent to the experimental data [23, 24] between 0.18 and 0.2.

Shown as Fig. 4(a) are the normalized mean pressure distributions $\langle p_w \rangle / p_\infty$ on the cylinder surface calculated by using DES, LES, and CLES. It appears that the mean wall pressures predicted by LES, DES and CLES are nearly identical to each other and coincide with the experimental data reported by Rodriguez [24] except for the range around the separation points (*i.e.*, $65° < \theta < 95°$). The result obtained in LES with a higher resolution of $257 \times 257 \times 61$ by Xu *et al.* shows a similar behavior, which is greatly improved when much finer-resolution grids ($513 \times 513 \times 121$) are used [21]. Therefore, it is inferred that the underestimation of the pressure by CLES near the extremum value point comes from the coarse mesh spacing. It is argued that the unsteady disturbances stemming from the vortex street decrease gradually from the separation point to the front stagnation point in weakly compressible flow, but diminish quickly before the separation point for flow with attached shock waves, which prevent the downstream perturbations from passing around the cylinder [24]. Fig. 4(b) shows the distribution of normalized rms pressure fluctuations p'_{rms}/p_∞ on the cylinder surface. As can be seen, the rms values of pressure fluctuations calculated in the present LES, DES, and CLES show little distinctions and are in good agreement with the experimental data except in the vicinity of the rear stagnation point, where the experimental values decrease gradually to a local minimum. We plot in Fig. 4(c) the distribution of time-averaged skin friction coefficient $\langle C_f \rangle$ obtained in
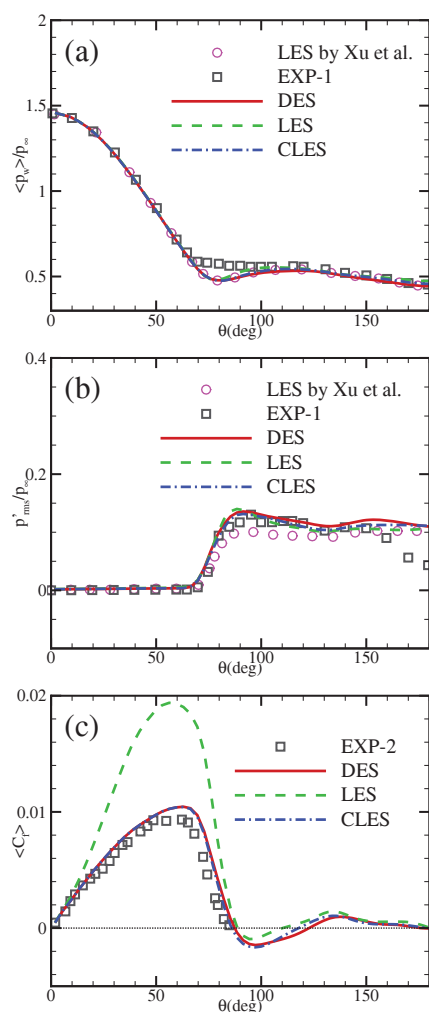
Figure 4: Distributions of (a) the normalized mean wall pressure $\langle p_w \rangle / p_\infty$, (b) the normalized rms pressure fluctuation p'_{rms} / p_∞, and (c) skin friction coefficient $\langle C_f \rangle$ calculated in the present simulations: DES (solid lines), LES (dashed lines) and CLES (dashed-dotted lines). In panels (a) and (b), the LES data by Xu *et al.* [21] (circles) and experimental data (squares) by Rodriguez [24] are plotted for comparison. In panel (c), the experimental data (squares) by Murthy and Rose [23] are plotted for reference. $\theta = 0°$ is located at the front stagnation point.

the present calculations. It is obvious that the friction forces predicted by DES and CLES are very close to the experimental results published by Murthy and Rose [23] with θ in the range of $0° \sim 90°$, while that from the present LES is about twice as large as the experimental value. The mean separation point can be determined from $\langle C_f \rangle$ distributions. The results are listed in Table 1. The CLES method gives the most accurate estimation (about $86.1°$) as compared with the experimental value of $\theta \simeq 85°$, while the present LES makes the worst prediction. Since the total drag force is dominated by the wall pressure,
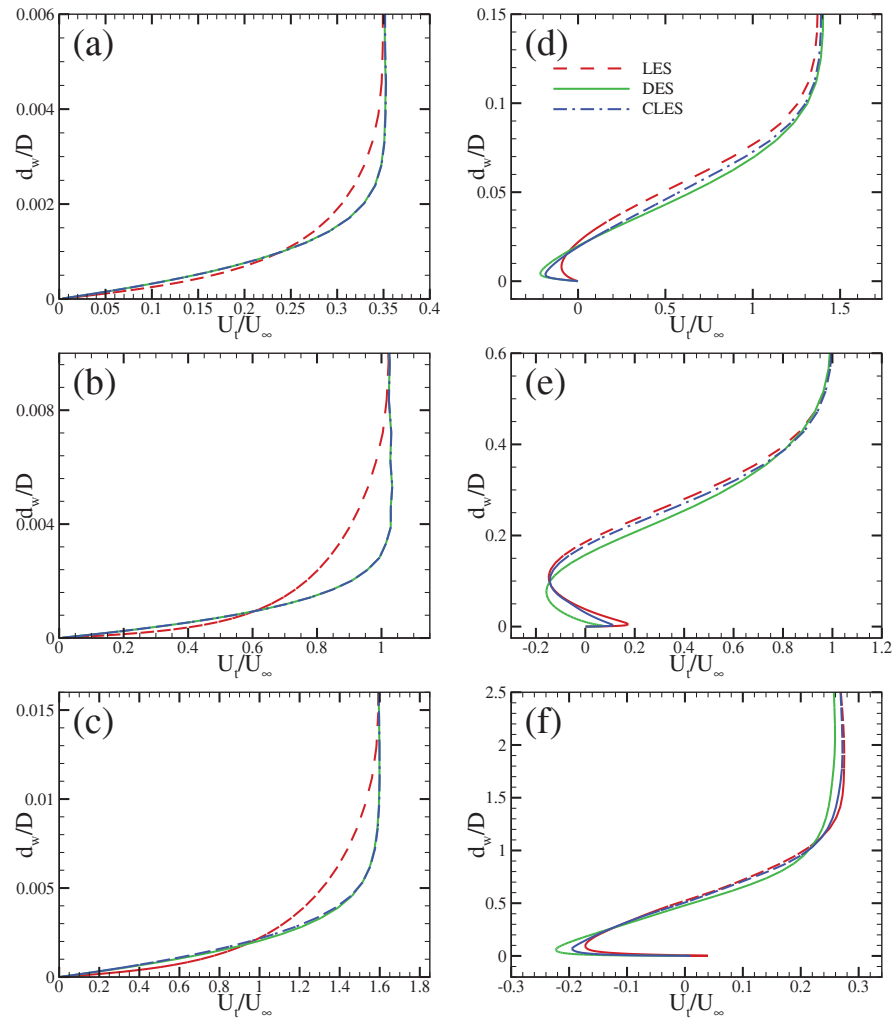
Figure 5: Mean tangential velocity profiles in the radial direction at six angular positions: (a) $\theta = 15°$, (b) $\theta = 45°$, (c) $\theta = 75°$, (d) $\theta = 105°$, (e) $\theta = 135°$, and (f) $\theta = 165°$ obtained in LES (dashed lines), DES (solid lines), and CLES (dashed-dotted lines). Here, d_w is the local distance to the cylinder surface and $\theta = 0°$ is located at the front stagnation point.

the overestimation of skin friction has little influence on the drag prediction.

We show in Fig. 5 the mean tangential velocity profiles in the radial direction at six angular positions, *i.e.*, (a) $\theta = 15°$, (b) $\theta = 45°$, (c) $\theta = 75°$, (d) $\theta = 105°$, (e) $\theta = 135°$, and (f) $\theta = 165°$. Here, d_w is the local distance to the cylinder surface. Before the mean separation point, the mean tangential velocities (U_t) calculated from DES and CLES nearly coincide with each other, while the mean tangential velocities calculated in LES deviate strongly from those in DES and CLES, especially in regions a little farther away from the cylinder surface (see Fig. 5(a), (b) and (c)). The profile from LES is much steeper than those from DES and CLES in the near wall region, being consistent with the larger value of $\langle C_f \rangle$
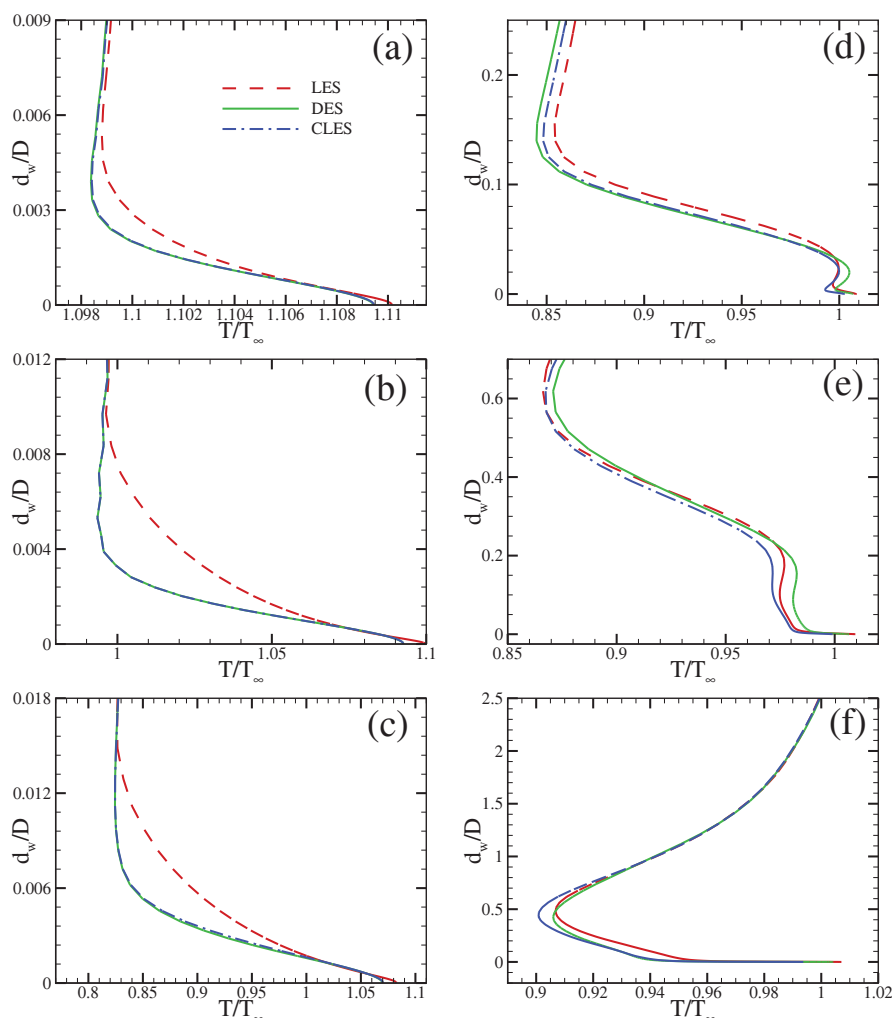
Figure 6: Mean temperature profiles in the radial direction at six angular positions: (a) $\theta = 15°$; (b) $\theta = 45°$; (c) $\theta = 75°$; (d) $\theta = 105°$; (e) $\theta = 135°$ and (f) $\theta = 165°$ obtained in LES (dashed lines), DES (solid lines), and CLES (dashed-dotted lines). $\theta = 0°$ is located at the front stagnation point.

observed in LES. The thickness of the local boundary layer calculated from LES is much thicker than those calculated from DES and CLES. There is no doubt that the proposed constraints on Reynolds stress and heat flux allow CLES to achieve better performance than traditional LES with the same grid resolution. After the separation point, the mean tangential velocity profile predicted by DES begins to depart from that by CLES, especially in the near-wall backflow region (see Fig. 5(d), (e) and (f)). Similar patterns are observed for the mean temperature profiles shown in Fig. 6 at the same angular positions as in Fig. 5. Before the separation point, the mean temperature given by traditional LES is higher than those from DES and CLES. After the separation point, the mean temperature
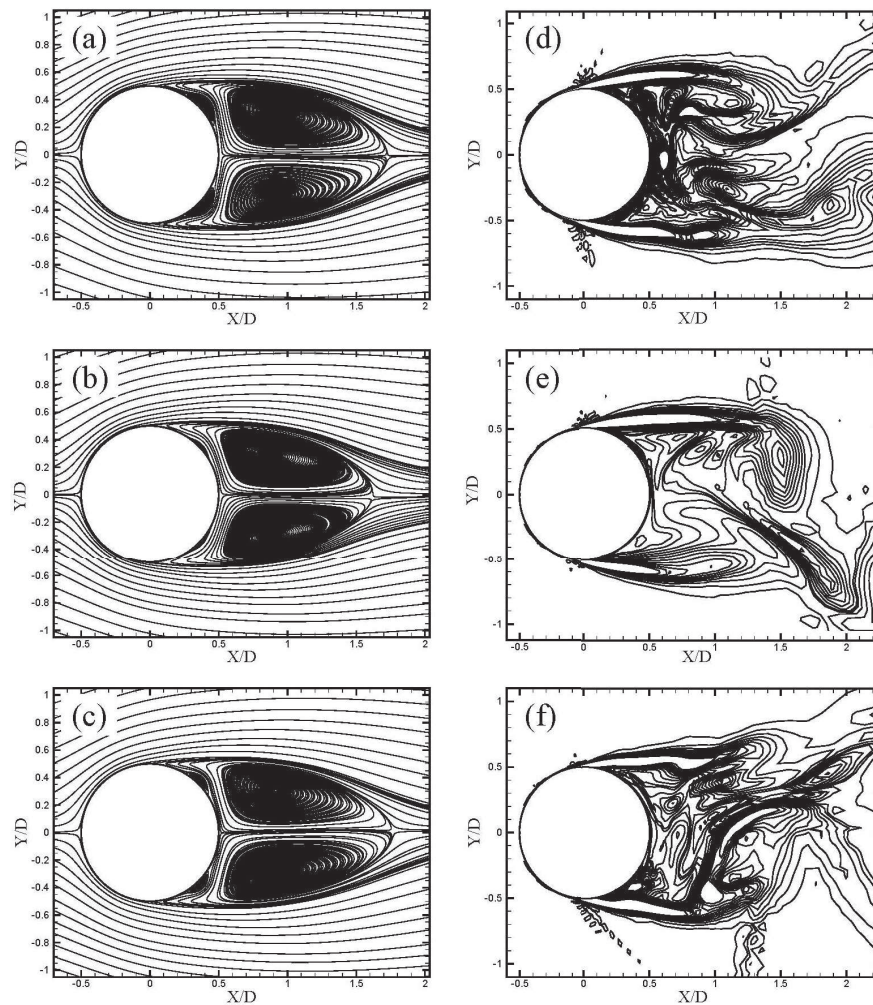
Figure 7: (a, b, c) Time-averaged streamlines and (d, e, f) instantaneous contours of spanwise vorticity in the central cross-section plane for flow past a circular cylinder obtained from LES (a, d), DES (d, e), and CLES (c, f).

profile predicted by DES shows apparent deviation from that by CLES in the near-wall backflow region, where the inflection points of temperature can be observed.

Shown in Fig. 7 (a)-(c) are ensemble-averaged (averaging in both time and spanwise direction) streamlines in the cross-section plane near the wall obtained from LES, DES, and CLES, respectively. Similar flow patterns, such as the main recirculation bubbles, small attached vortices, *etc.*, are observed for the flow fields obtained from the three simulations. The recirculation lengths calculated from LES and CLES are approximately equal to each other (around 1.2D), and are a little longer than that from DES (about 1.1D). The size of the attached vortices on the lee side of the circular cylinder observed in CLES is

larger than that in DES, but is smaller than that in LES. This is similar to the correspond-
ing results for incompressible case [30]. To gain further insight into the instantaneous
flow structures in the near-wall and near-wake regions, we display in Fig. 7 (d)-(f) the
contours of instantaneous spanwise vorticity for the central cross-section slice obtained
from LES, DES, and CLES, respectively. As can be expected, CLES possesses the same in-
herent property as traditional LES in predicting the "small-scale" fluctuating flow struc-
tures in the wake region. In DES, however, the RANS solution in the near-wall layer has
significant influence on the flow patterns in the wake, which, though solved using LES,
look much smoother than those observed in LES and CLES. Therefore, the compressible
CLES method employed in the present simulations shares the positive properties from
both traditional LES and DES in predicting compressible separated flows at acceptable
computational cost.

5   The dynamics of shock waves

In flow past a circular cylinder, the compressible effect is of great importance when the
free-stream Mach number is in certain subsonic or transonic range, since complex shock
waves are generated locally and interact with each other and with turbulence. In this
section, we qualitatively study the formation and propagation characteristics of shock
waves by analyzing the data obtained in CLES at Mach and Reynolds numbers of 0.75
and 2×10^5, respectively.

Show in Fig. 8 are six snapshots of 3D shock waves and vortex structures depicting
different developing stages within a vortex shedding cycle. The vortex structures are
identified by the isosurfaces of the second invariant of the strain rate tensor (Q) with
$Q = 1.0$, while the shock waves are detected by using the surface method proposed by
Pagendarm *et al.* [48], in which the shock position is determined by the maximal pressure
gradient in the local streamwise direction, and a thresholding technique is employed to
distinguish significant portions of the shock patterns from weak numerical artifacts with
a threshold value of 0.75. It is clearly seen from Fig. 8 that there are three types of shock
waves, *i.e.*, the shock waves around the cylinder (denoted S1), the shock waves embed-
ded "on" the shear layer (denoted S2), and the shocklets in the wake region (denoted
S3). We first look at the upper part of the flow domain. In Fig. 8 (a), we can see that
shock wave S2 is very strong (for a 2D view, see Fig. 10), and occupies nearly the whole
spanwise width of the cylinder. In the meantime, shock wave S1 begins to emerge, but
is still weak and discontinuous. As time goes on, shock wave S1 moves upstream and
grows stronger, while shock wave S2 bends upward (see Fig. 8 (b)). Furthermore, shock
wave S1 becomes much stronger and interacts with shock wave S2 as shown in Fig. 8 (c).
Then, shock wave S2 gets distorted and broken due to the interferences from the vortex
structures in the shear layer and shock wave S1 (see Fig. 8 (d)). After that, shock wave
S2 breaks into small and weak pieces and shock wave S1 bends upward as seen in Fig. 8
(e). Soon later, both shock wave S1 and shock wave S2 become weaker and weaker and
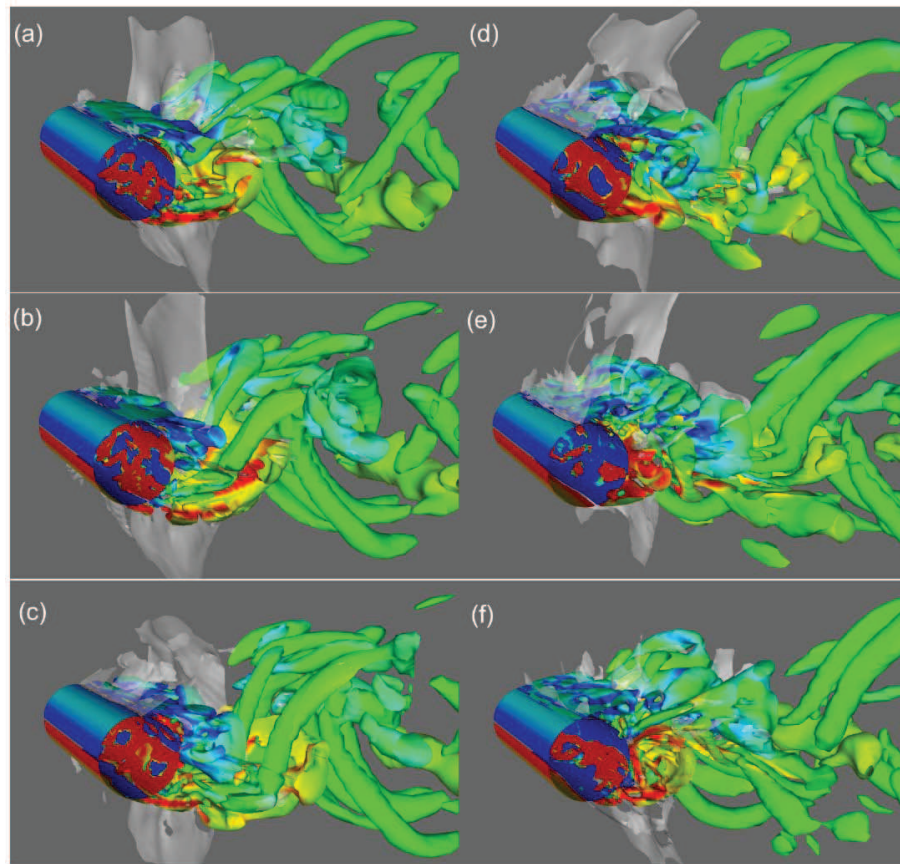
Figure 8: Snapshots of 3D shock waves and vortex structures at six successive moments within a period of vortex shedding extracted from CLES.

almost disappear as shown in Fig. 8 (f). The motion and propagation of shock waves in the lower part experience a similar process to those observed in the upper part with a time delay. There also exist complicated interactions between the shocklets and vortex structure in the wake region of the flow domain, which can be seen more clearly in Fig. 10.

The appearance of the shock waves implies that there shall be supersonic regions in the flow domain, though the free-stream velocity is subsonic. We show in Fig. 9 the instantaneous isocontours of the local Mach number (M_l) for the six time slices corresponding to those shown in Fig. 8. It is observed that there are always local supersonic zones above/under the shear layers and in the wake, which are believed to be associated with the local strong turbulent fluctuations. The positions of the supersonic zones exhibit the same periodicity as that for vortex shedding.

In order to see the shock wave/turbulence interaction more clearly, especially in the wake region, we display in Fig. 10 the instantaneous contours of the dilatation θ (*i.e.*, the
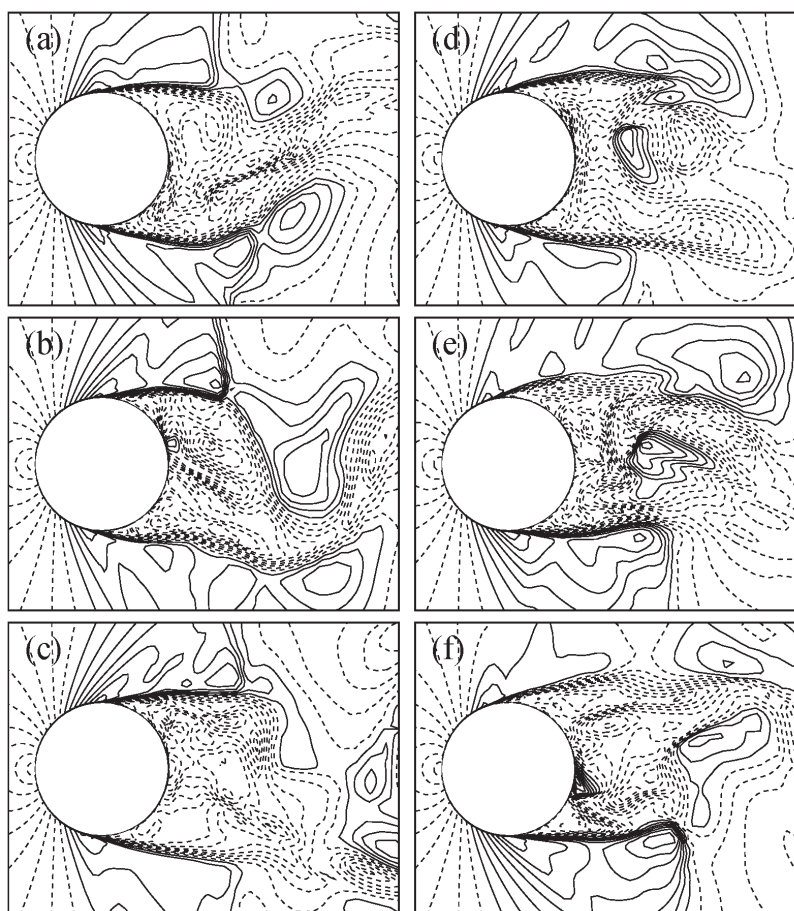
Figure 9: Instantaneous isocontours of the local Mach number (M_l) in the central cross-section plane at the same successive moments as in Fig. 8 obtained from CLES. Solid contour lines indicate the supersonic regions ($M_l > 1$), and dashed contour lines represent the subsonic regions ($M_l < 1$).

divergence of the velocity field, flood) together with those of the spanwise vorticity ω_z (lines) in the central cross-section plane at the same time series as shown in Fig. 8. Here, regions with $\theta < -1$ are identified as the locations where shock waves occur. As we can see previously in Fig. 8, the formation and disappearance of shock waves S1 and S2 in the lower side of the cylinder are similar to those in the upper side, and happen alternatively and periodically in time. The flow separates from the cylinder surface, forming a shear layer, which flaps around the cylinder surface and induces the formation of a Kármán vortex street. One end of shock wave S2 lies on the shear layer and moves up and down with it. There exist complex interferences between shock S2 and the shear layer. Shock wave S1 forms on the cylinder surface around the separation point. The flapping of the shear layer shall induce the oscillation of shock S1 along the cylinder surface, which in return accelerates the separation of the boundary layer. It can also observed in Fig. 10
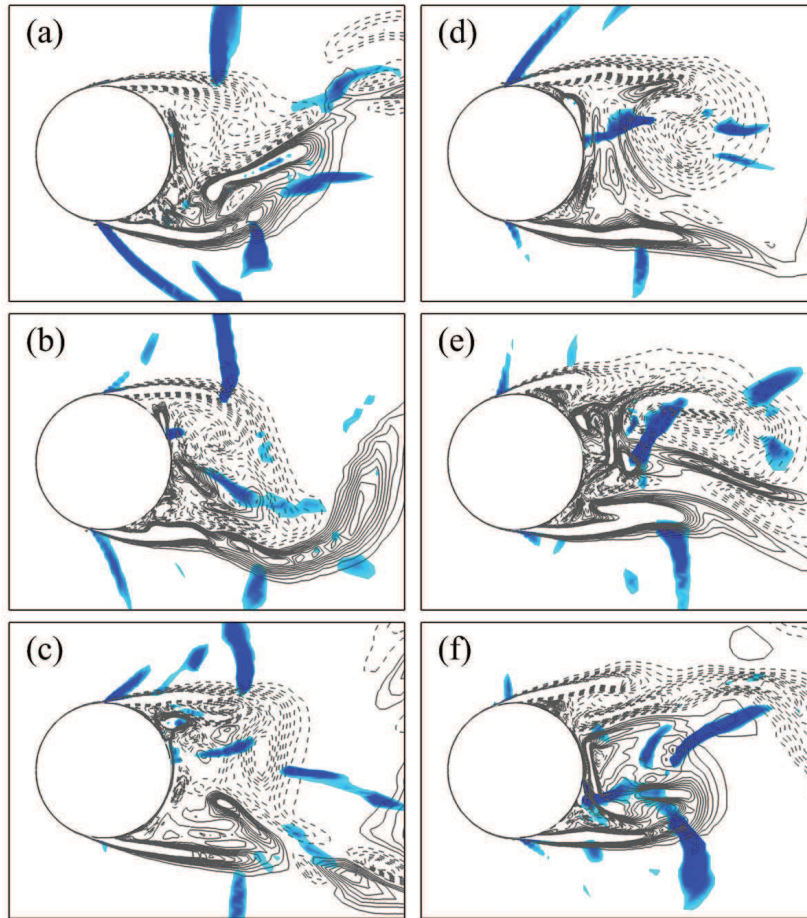
Figure 10: Instantaneous isocontours of the dilatation $\theta = \partial \tilde{u}_i / \partial x_i$ (flood for $\theta < -1$) and the spanwise vorticity (solid lines for positive values and dashed for negative values) for the same slices both in time and in space as shown in Fig. 9.

that shocklets (S3) form in the near wake region of the cylinder, characterized by strong negative dilatation [49, 50]. As discussed by Xu *et al.* [21], these shocklets interact mutually with the turbulence in the wake. The presence of shocklets stimulates a higher level of turbulence intensity, and meanwhile the strong turbulent fluctuations increase the possibility of the formation of shocklets.

6 Mach number effects

For compressible flow past a circular cylinder, free-stream Mach number has a significant influence on the flow pattern and the statistical quantities of interest. In this section, we investigate the role of the Mach number on compressibility effects by using the

Table 2: Some integral quantities obtained in CLES at various free-stream Mach numbers.

Ma	C_D	C_{Lrms}	St	θ_{sep}	L_r/D
0.1	0.778	0.399	0.268	105.8°	0.383
0.3	0.682	0.168	0.270	94.8°	1.01
0.5	1.206	0.659	0.210	85.2°	0.566
0.75	1.571	0.287	0.188	86.1°	1.24
0.95	1.839	0.0046	-	107.7°	1.25

compressible CLES method over a wide range of free-stream Mach number from the incompressible limit ($Ma=0.1$) to the upper transonic limit ($Ma=0.95$). The five selected simulation cases and the corresponding integral quantities are listed in Table 2. Other input parameters in the simulations are the same as those utilized in Section 4.

If one assumes that the flow along the streamline ahead of the front stagnation point is isentropic, the stagnation pressure can be theoretically estimated by $p_{sp} = (1 + \frac{\gamma-1}{2}Ma^2)^{\frac{\gamma}{\gamma-1}} p_\infty$, which implies that the mean pressure coefficient $\langle C_p \rangle$ increases monotonically with the increasing Mach number, and is demonstrated by the numerical results in Fig. 11 (a) where the distributions of mean surface pressure (given by mean pressure coefficient $\langle C_p \rangle = 2(p_w - p_\infty)/\rho_\infty U_\infty^2$) calculated in CLES at various Mach numbers are plotted. In the adverse pressure gradient region, the pressure gradient keeps decreasing when Mach number increases. Angular position of the minimum pressure coefficient first moves toward the front stagnation point and then moves back away from that point as Mach number changes from 0.1 to 0.95. The plateau value of the pressure coefficient, which is achieved on the lee side of the cylinder, increases first and then decreases with the increasing Mach number. The Mach number, which distinguishes the opposite behaviors of pressure coefficient mentioned above, is between 0.3 and 0.5, and is called subcritical Mach number and denoted by M_{sc}.

Fig. 11 (b) shows the angular distribution of the rms pressure fluctuations p'_{rms}/p_∞ along the cylinder surface for CLES at various Mach numbers. When Ma is less than M_{sc}, p'_{rms} increases gradually from the front stagnation point to a point where it reaches the maximum value, and then decreases slowly to form a plateau on the lee side of the cylinder. It ought to be mentioned that we can hardly see the pressure fluctuations when $Ma=0.1$, since p_∞ is relatively larger in weak compressible flow than in strong compressible case. When the Mach number is larger than M_{sc}, the rms value of the pressure fluctuations dramatically increases prior to separation and continuously decays to a plateau after the mean separation point. The sudden change of p'_{rms} around the separation point is consistent with the experimental observations by Rodriguez [24], who attributed this phenomenon to the formation of shock waves on the cylinder surface. It is argued that the oscillating shock waves can prevent the downstream perturbations from propagating upstream around the cylinder and result in a strong reduction in the unsteady pressure intensity cross the separation point. Therefore, it is inferred that no apparent shock wave
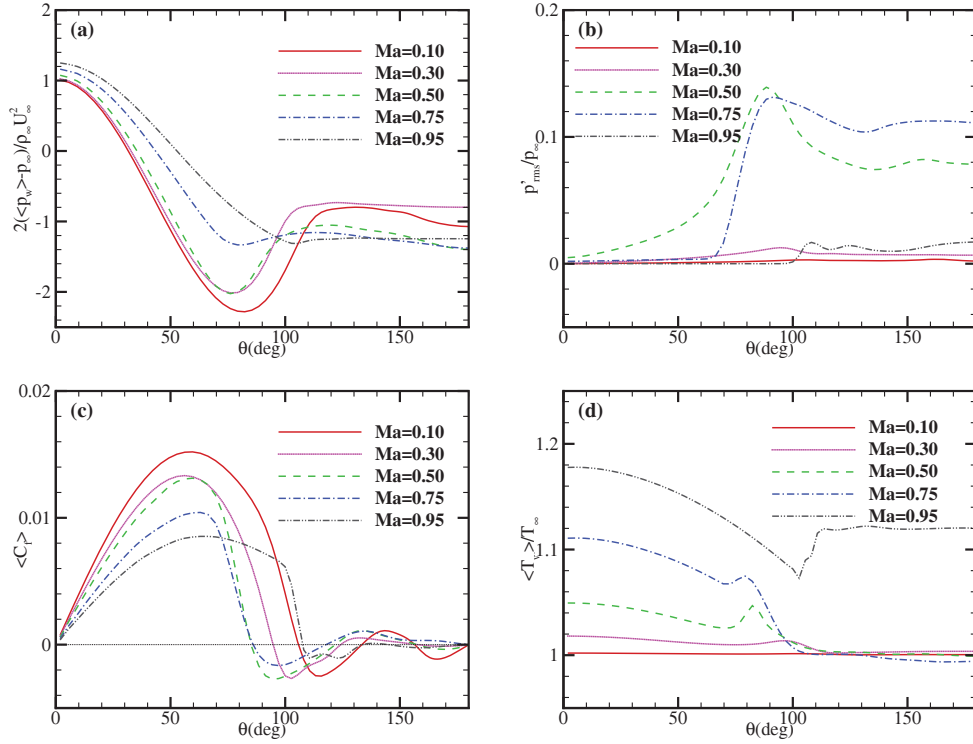
Figure 11: Distributions of (a) the mean wall pressure coefficient $\langle C_p \rangle = 2(p_w - p_\infty)/\rho_\infty U_\infty^2$, (b) the rms pressure fluctuations p'_{rms}/p_∞, (c) the mean skin friction coefficient $\langle C_f \rangle$, and (d) the mean wall temperature $\langle T_w \rangle / T_\infty$ obtained in CLES at different free-stream Mach numbers: Ma=0.1 (solid lines), Ma=0.3 (dotted lines), Ma=0.5 (dashed lines), Ma=0.75 (dashed-dotted lines), and Ma=0.95 (dashed-double-dotted lines). Here, $\theta = 0°$ indicates the front stagnation point.

structures appear when free-stream Mach number is below the subcritical Mach number M_{sc}.

We show in Fig. 11 (c) the mean skin friction coefficient $\langle C_f \rangle$ calculated in CLES for different free-stream Mach numbers. As Mach number increases, it is found that the separation point (*i.e.*, the angular position where $\langle C_f \rangle$ first changes its sign) move toward the front stagnation point along the cylinder wall when Ma is less than M_{sc}, and move toward the rear stagnation point when Ma is larger than M_{sc}. The variation trend of the primary separation angle θ_{sep} with respect to Mach number Ma can be seen in Table 2. It shall be mentioned also that the skin friction coefficient decreases monotonically as Mach number increases in the range of interest before the maximum value.

Shown as Fig. 11 (d) are the mean wall temperature profiles along the cylinder surface obtained for CLES of flows at various Mach numbers. It is seen that the wall temperature, and thus the wall viscosity at the same angular position, increases as the Mach number increases prior to the mean separation point, showing an opposite tendency to that of skin friction coefficient. Therefore, the velocity gradient on most of the windward wall
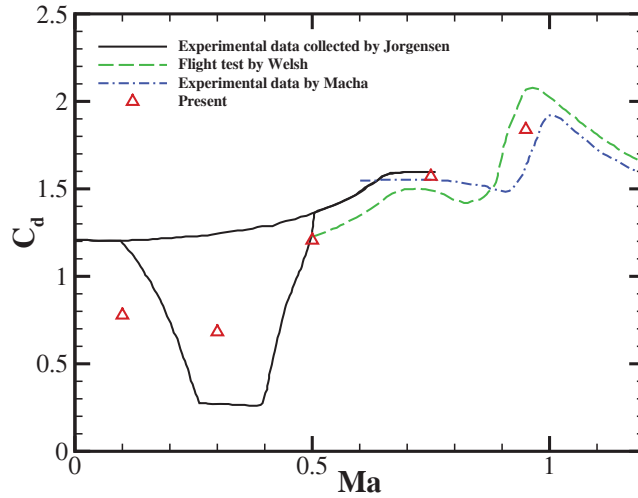
Figure 12: Drag coefficient versus the free-stream Mach number obtained from the present CLES (triangles), the experimental measurement by Jorgensen (solid lines) [51], the flight test by Welsh (dashed line) [52], and the experimental measurement by Macha (dashed-dotted line) [53]. The Reynolds numbers for the cited experiments range from $\sim 10^5$ to $\sim 10^6$.

shall keep decreasing as Mach number increases, except for the upper transonic limit. For given Mach number below 0.95, there exists a inflection point on the temperature profile, after which the mean wall temperature increases quickly to a local maximum value at the mean separation point, and then decays identically to the temperature of inflow (T_∞). The existence of inflection point is believed to be closely related to the flow separation phenomena and the oscillating shocks on the cylinder surface. When Mach number approaches the upper transonic limit (*e.g.*, $Ma = 0.95$ considered in this paper), the variation trend of the mean wall temperature beyond the inflection point is rather different from the subsonic cases. The mean wall temperature increases suddenly to a larger value around the separation point and remains unchanged when traveling toward the rear stagnation point, which may attribute to the quasi-steady recirculation zone formed in the lee side of the cylinder.

The drag force on the cylinder is directly related to the pressure distribution along the cylinder surface shown in Fig. 11 (a). As can be seen in Table 2, the drag coefficient exhibits an opposite trend to plateau value of the wall pressure when Mach number increases from 0.1 to 0.95, *i.e.*, decreasing when $Ma < M_{sc}$ and increasing when $Ma > M_{sc}$. The diverse responses of the drag coefficient to the Mach number in different ranges agree with the experimental data reported previously [51–53] as shown in Fig. 12. Here, the total drag is approximated by integrating the pressure around the cylinder surface, since the friction force is negligibly small. It should be emphasized that although the Reynolds numbers for these experimental measurements vary from $\sim 10^5$ to $\sim 10^6$, these experimental data provide a consistent and trustable reference for comparison.

Listed also in Table 2 are some other statistical quantities calculated in CLES at differ-

ent Mach numbers. With the increase of Mach number, the Strouhal number St increases when Ma is less than M_{sc}, and then decreases. Both the rms lift coefficient fluctuations C_{Lrms} and the recirculation length L_r show a three-stage response to the continuously changed Mach numbers. The anomalous behaviors of these quantities are worth further investigation.

7   Wall temperature effects

It has been demonstrated both experimentally [54] and numerically [55] that the temperature field has an important influence on the flow pattern of compressible laminar flow past a heated circular cylinder, especially when the ratio of the cylinder surface temperature (T_w) to the free-stream temperature (T_∞), denoted by $T^* = T_w/T_\infty$, exceeds 1.1. In this section, the effects of wall temperature on compressible flow past a heated circular cylinder are investigated by using CLES method. Three different wall temperatures are chosen by setting T^* equal to 0.4 (cooling wall), 1.0 (neutral wall), and 2.0 (heating wall), respectively. The free-stream Mach number ($Ma = 0.75$), Reynolds number (2×10^5), and other input parameters and numerical setup for CLES are the same as those utilized in Section 4, except that isothermal wall boundary condition is employed in this study.

We display in Table 3 several typical quantities calculated in CLES using different wall temperatures. The corresponding results obtained by using the adiabatic wall boundary condition are also provided for comparison. These quantities include the drag coefficient C_D, the rms lift coefficient fluctuations C_{Lrms}, the Strouhal number St, the mean separation angle θ_{sep}, the recirculation length L_r, and the pressure coefficient at the rear stagnation point C_{pb}. It is found that when the cylinder surface is changed from cooling wall to heating wall, C_D, C_{Lrms}, and θ_{sep} decrease monotonically, while L_r and C_{pb} show an opposite tendency. However, the Strouhal number remains unchanged in regard to the increasing T^*. In other words, the vortex shedding frequency are hardly affected by the wall temperature in high Reynolds number compressible flows past a circular cylinder. This is in sharp contrast to the low Reynolds number case [54, 55], in which St decreases identically with the increasing value of wall temperature.

Shown in Fig. 13 (a)-(d) are the distributions of the normalized mean wall pressure $\langle p_w \rangle / p_\infty$, the normalized rms value of the pressure fluctuations p'_{rms}/p_∞, the mean skin

Table 3: Comparison of some statistical quantities obtained in CLES with adiabatic and isothermal wall boundary conditions.

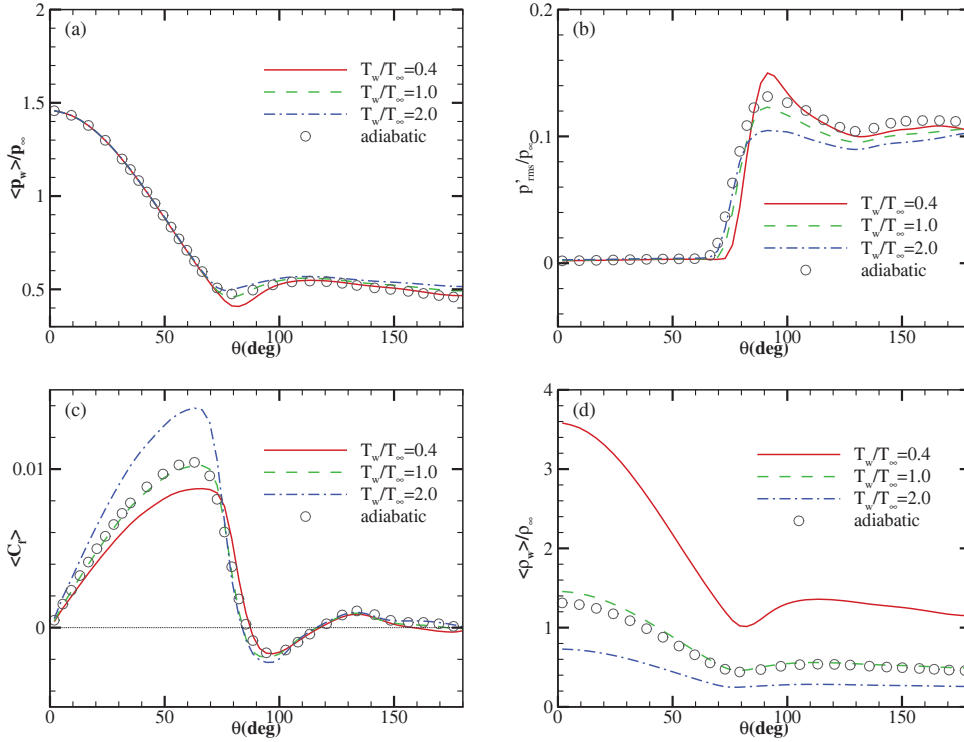| Case	C_D	C_{Lrms}	St	θ_{sep}	L_r/D	C_{pb}
Adiabatic	1.571	0.287	0.188	86.1°	1.24	0.458
$T^* = 0.4$	1.572	0.277	0.190	87.4°	1.20	0.467
$T^* = 1.0$	1.538	0.256	0.190	84.2°	1.38	0.492
$T^* = 2.0$	1.510	0.228	0.190	83.8°	1.52	0.515

Figure 13: Distributions of (a) the mean wall pressure $\langle p_w \rangle / p_\infty$, (b) the rms pressure fluctuations p'_{rms} / p_∞, (c) the mean skin friction coefficient $\langle C_f \rangle$, and the mean wall density $\langle \rho_w \rangle / \rho_\infty$ obtained in CLES with isothermal wall boundary conditions. The results with adiabatic wall boundary condition are also displayed for comparison. $\theta = 0°$ is located at the front stagnation point.

friction coefficient $\langle C_f \rangle$, and the normalized mean wall density $\langle \rho_w \rangle / \rho_\infty$, respectively, along the cylinder surface obtained in CLES with isothermal and adiabatic wall boundary conditions. We can see from Fig. 13 (a) that the mean wall pressures for different thermal boundary conditions are almost the same when $\theta \lesssim 70°$. For a given angular position when $\theta > 70°$, the mean pressure increases for increasing values of wall temperature or T^*. The discrepancies among the pressures after the points of separations account for the variations in drag coefficients due to the differences in wall temperature listed in Table 3.

The rms pressure fluctuations for isothermal wall conditions (lines) plotted in Fig. 13 (b) show a similar trend to those for adiabatic wall condition (circles). The rms value of the pressure fluctuations suddenly increases to a local peak after separation occurs and continuously decays to a plateau on the lee side of the cylinder. The higher the wall temperature, the lower the plateau.

The mean skin friction coefficient $\langle C_f \rangle$ is significantly influenced by the wall temperature before the mean separation point as shown in Fig. 13 (c). For a given θ in the range between $0°$ and $70°$, the friction coefficient increases for increasing values of the wall temperature. As an illustration, we plot in Fig. 14 the mean tangential velocity profiles for
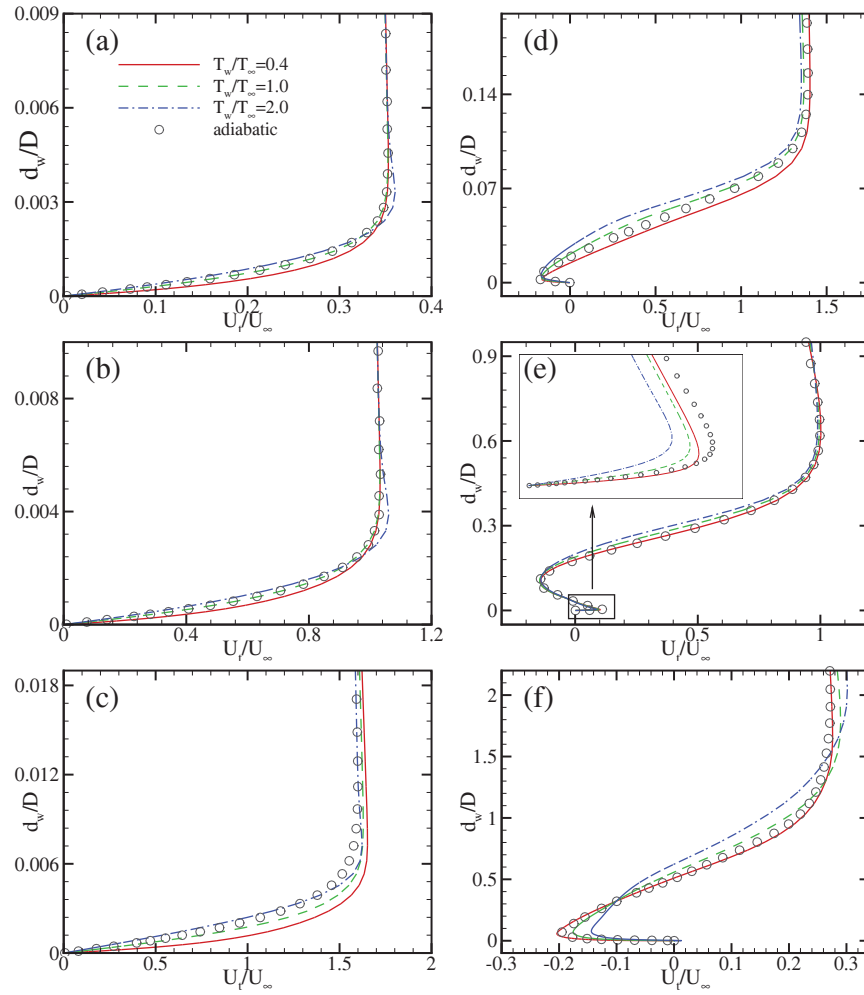
Figure 14: Mean tangential velocity profiles in the radial direction at six angular positions: (a) $\theta = 15°$, (b) $\theta = 45°$, (c) $\theta = 75°$, (d) $\theta = 105°$, (e) $\theta = 135°$, and (f) $\theta = 165°$ obtained in CLES with isothermal and adiabatic wall boundary conditions. $\theta = 0°$ is located at the front stagnation point.

different thermal boundary conditions at six angular positions. As can be seen, the velocity gradients in the radial direction show slight difference on the cylinder surface. In fact, the velocity gradient decreases with the increasing of the wall temperature when one zooms in very close to the wall. According to the Sutherland's law (see Eq. (2.7)), the viscosity for the heating wall case and cooling wall case are $\mu_h \simeq 1.65\mu_\infty$ and $\mu_c \simeq 0.44\mu_\infty$, respectively. Therefore, it is the significant change in viscosity that compensates the deficit of velocity gradient and contributes dominantly to the apparent discrepancies in $\langle C_f \rangle$ before the point of mean separation. The slight differences in $\langle C_f \rangle$ after the separation point come from the balance between the velocity gradients (see Fig. 14 (d)-(f)) and the viscosities. It is interesting to note that although $\langle C_f \rangle$ is largest for the heating wall case,
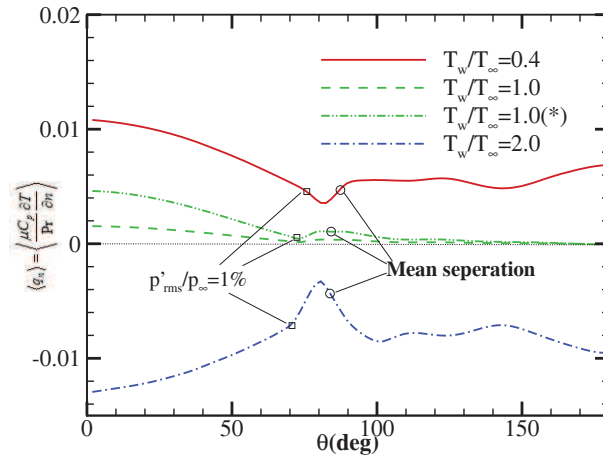
Figure 15: Distributions of the mean heat fluxes on the cylinder surface obtained in CLES with different thermal wall boundary conditions. The legend "$T_w/T_\infty=1.0(*)$" indicates that the heat fluxes are amplified by a factor of 3 for clarity. $\theta=0°$ is located at the front stagnation point.

the drag coefficient C_D is smallest in contrast. This is attributed to the largest pressure on the lee side of the heating cylinder as shown in Fig. 13 (a) and reveals that the wall pressure contributes dominantly to the total drag force. Another conclusion drawn from Fig. 13 (c) is that the higher wall temperature leads to earlier flow separation (see the mean separation angle list in table 3), and results in a longer recirculation domain.

The mean density distributions for various wall temperatures on the cylinder surface differ strongly from each other as shown in Fig. 13(d), but have similar shape to the mean wall pressure distributions. As the wall temperature increases, the mean density gets decreased. In accordance to the thermodynamical equation of state (see Eq. (2.4)), large variations in temperature will give rise to large variations in density (in the opposite direction), since the changes in pressure are quite small.

Fig. 15 shows the distributions of the mean heat fluxes on the cylinder surface calculated in CLES with different wall temperatures. Here, a positive value means that heat flows out from the flow field and is transferred into the cylinder through the cylinder surface. When $T^*=0.4$, it is clearly seen that the mean heat fluxes are positive everywhere on the whole surface, implying that the heat flows into the cylinder through the whole cylinder surface. The cylinder acts as a cooling device for the flow field. When the wall temperature is increased such that $T^*=1.0$, the heat fluxes are still positive on most part of the cylinder surface except for the negligibly small negative values around the rear stagnation point (see the amplified line). Such a cylinder, called neutral wall cylinder in this paper, acts as a cooling device in most regions, but acts as a heating device near the rear stagnation point. When $T^*=2.0$, however, the heat fluxes are negative everywhere on the cylinder surface, indicating that heat flows into the flow field through the whole cylinder surface, and the cylinder acts as a heating device for the flow field.

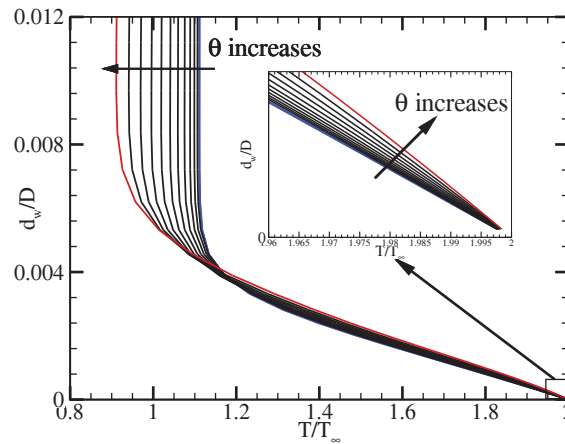For all three isothermal wall boundaries, the absolute values of mean heat fluxes on

Figure 16: Mean temperature profiles along the radial direction at different circumferential positions ranging from $0°$ to $60°$ with an increment of $\delta\theta = 5°$ obtained in CLES with heating wall boundary ($T^* = 2.0$). $\theta = 0°$ is located at the front stagnation point.

the cylinder surface decrease continuously from the maximum at the front stagnation point to a local minimum at a circumferential position before the mean separation point, and then show a short-range increase to reach a local maximum. After that, the absolute values of mean heat fluxes decay gradually to zero for the neutral wall case, and form a plateau for the cooling and heating wall cases. The relative distances between the onset position of separation ($p'_{rms}/p_\infty = 1\%$, see squares in Fig. 15) and the mean separation position measured in the three cases are different from each other, with the largest for the heating wall case and the smallest for the neutral wall case. The local minimum and maximum values are closely related to the instantaneous separation phenomenon, which induces drastic changes in pressure fluctuation (see Fig. 13 (b)). The monotonic decrease in the mean heat fluxes in the circumferential direction before the onset position is believed to be caused by the decrease in the temperature gradient in the wall-normal direction. Shown in Fig. 16 are the mean temperature profiles along the wall-normal direction at various circumferential angles ranging between $0°$ and $60°$. It is clearly seen from the zoom for near-wall profiles the temperature gradients in the wall-normal direction get reduced with increasing circumferential angle θ as conjectured. It can also be found that the heat boundary layer keeps growing thinker and the mean temperature in the outer layer of the heat boundary gets lower when one travels from the front stagnation point to the onset point of flow separation.

In fact, the influences of different thermal wall boundary conditions on the flow and temperature patterns are mainly concentrated in the near-wall regions of the flow field, and can be neglected in regions far away from the cylinder surface. Shown in Fig. 17 are the snapshots (isocontours) of mean temperature around the circular cylinder obtained in CLES with four different thermal wall boundary conditions, *i.e.*, three isothermal walls with $T^* = 0.4$ (Fig. 17 (a)), $T^* = 1.0$ (Fig. 17 (b)), $T^* = 2.0$ (Fig. 17 (c)), and an adiabatic wall
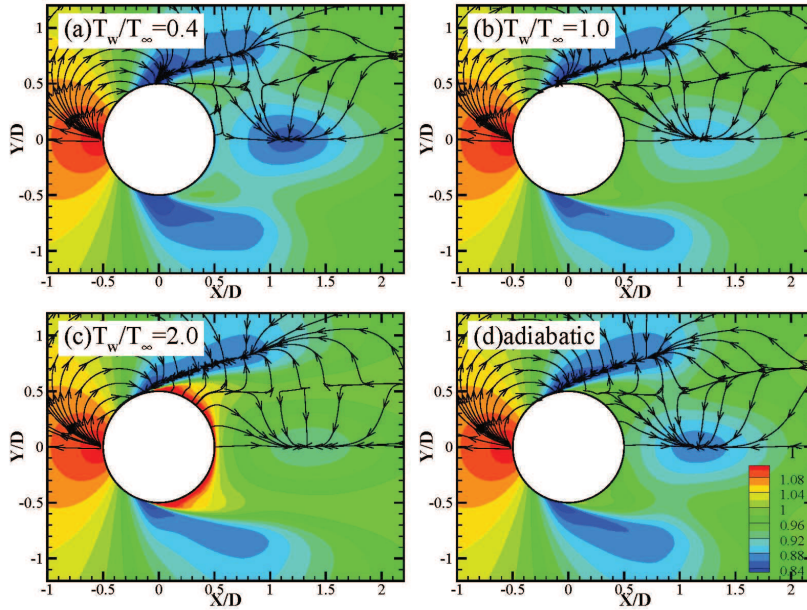
Figure 17: Snapshots of the mean temperature field around the circular cylinder for different thermal wall boundary conditions: (a) $T_w/T_\infty = 0.4$, (b) $T_w/T_\infty = 1.0$, (c) $T_w/T_\infty = 2.0$, and (d) adiabatic wall. The lines with arrows in the upper half of the panels show the directions of the heat fluxes.

(Fig. 17 (d)). The solid lines with arrows in the upper half panels indicate the directions of mean heat fluxes. It is obvious that the heat fluxes in the four panels are almost the same to the eyes, with a source near the front stagnation point, a sink near the mean separation point, and a sink in the center wake with $x/D \sim 1.2$. There exists a saddle point between these two sinks, from which heat flows to the sinks. The detailed behaviors of the heat fluxes in the near-wall regions show a similar pattern as seen in Fig. 15, which can not be observed in this figure.

In order to study the effects of the thermal wall boundary conditions on the temperature distribution in near-wall regions of the cylinder, we plot in Fig. 18 the mean temperature profiles along the radial direction at six different angular positions using isothermal wall conditions (lines) and adiabatic wall condition (circles). It is clearly seen that the temperature profiles nearly coincide with each other when the distance to the wall d_w exceeds 1%D before the mean separation point. However, the influences of thermal wall boundary conditions can propagate much further in the radial direction after the mean separation point. For instance, the mean temperatures measured at $\theta = 135°$ for different thermal wall conditions still differ from each other at $d_w \sim 0.18D$ as can be found in Fig. 18 (e). This discrepancy in response to the thermal wall boundary conditions in the near-wall regions comes from the fact that the flow is relatively stable before the separation, and is chaotic after the separation. Similar conclusion can be drawn for the near-wall mean velocity profiles as shown in Fig. 14 and the mean density profiles (not shown here).
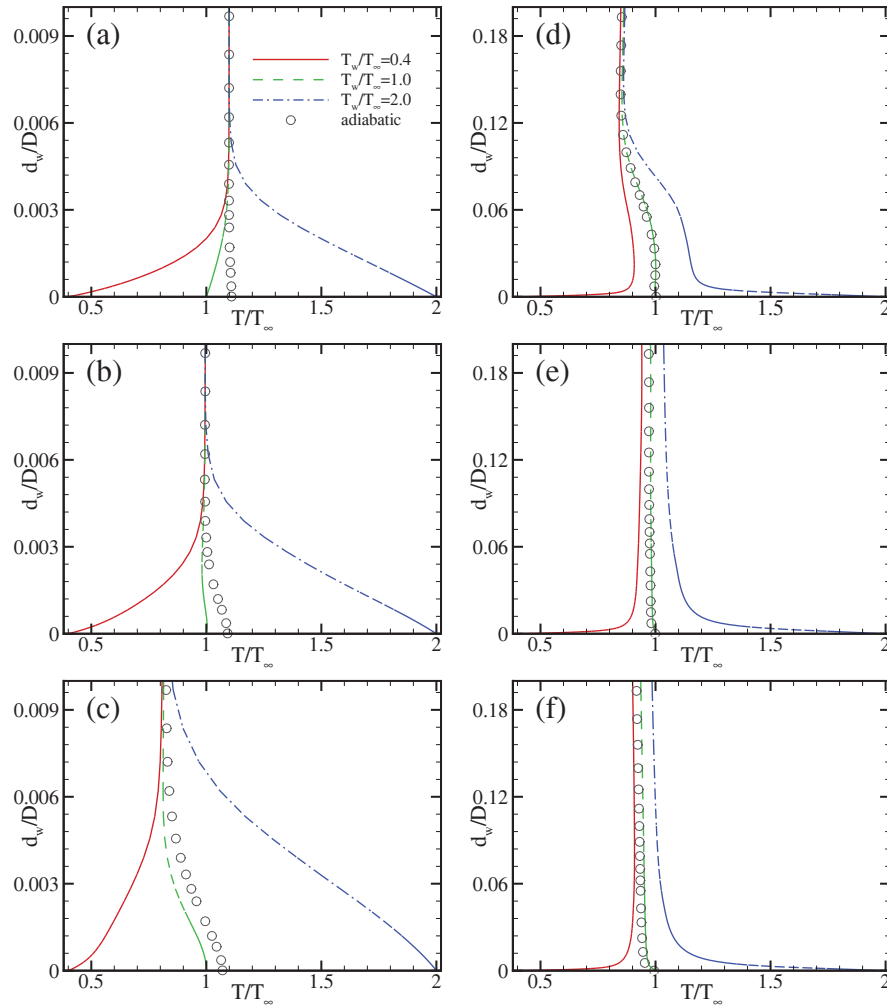
Figure 18: Mean temperature profiles along the radial direction at six angular positions: (a) $\theta=15°$, (b) $\theta=45°$, (c) $\theta=75°$, (d) $\theta=105°$, (e) $\theta=135°$, and (f) $\theta=165°$ obtained using CLES with different thermal boundary conditions. $\theta=0°$ is located at the front stagnation point.

8   Conclusions and discussions

In this paper, a recently developed constrained large-eddy simulation method for compressible flows [31] is used to investigate compressible flow past a circular cylinder at an inflow Reynolds number $Re=2\times10^5$ and various free-stream Mach numbers.

Firstly, The compressible CLES method is tested and validated by simulating compressible flow past a circular cylinder at a free-stream Mach number of 0.75 with adiabatic wall boundary condition. Typical integral and statistical quantities, including the mean drag coefficient, the rms lift fluctuations, the Strouhal number, the mean wall pres-

sure, the rms wall pressure fluctuations and the skin friction coefficient, are compared with those obtained in present DES and LES on the same mesh, the experimental data, and those reported by Xu *et al.* [21] using traditional LES method on a finer mesh. It is found that the CLES method combines the most positive aspects from traditional LES method and hybrid RANS/LES (*e.g.*, DES) method, respectively. With relatively coarser grid resolution and larger time step, CLES method can predict the realistic flow structures in the wake and reliable integral quantities as compared with those obtained in LES with much finer mesh [21]. The present DES fails to figure out the fluctuating structures in the near wake of the cylinder because of the smooth RANS solution close to the cylinder surface. The present LES, however, overestimates the skin friction coefficient by a factor of two, and fails to predict the mean velocity and temperature profiles along the radial direction due to the coarse resolution of the computation grids. The formation and propagation of three types of shock waves as well as shock wave/shock wave and shock wave/turbulence interactions are studied by visualizing the CLES data. It turns out that the CLES method can successfully simulate the complicated shock wave dynamics very well. Therefore, we believe that the present CLES method should be a promising tool for simulation of compressible wall-bounded turbulent flows with massive separations.

Secondly, Mach number effects on the flow patterns and typical aerodynamic quantities are studied with the free-stream Mach number varying from the incompressible limit ($Ma=0.1$) to the upper transonic limit ($Ma=0.95$). It is found that there exists a subcritical Mach number M_{sc} (between 0.3 and 0.5), at the which the mean separation angle achieves its minimum value. Main thermodynamic quantities obtained in the range of $Ma<M_{sc}$ show opposite variation trend to those in the range of $Ma>M_{sc}$. Some parameters, such as the rms lift coefficient fluctuations and the recirculation length, show a three-stage response to the increasing Mach numbers. The final stage behavior of these quantities shall be closely associated with the upper transonic effect, which is not investigated in detail in the present paper.

Finally, wall temperature effects on the flow and temperature fields as well as the aerodynamic quantities are investigated with three different isothermal wall boundary conditions, *i.e.*, a cooling wall ($T_w/T_\infty = 0.4$), a neutral wall ($T_w/T_\infty = 1.0$), and a heating wall ($T_w/T_\infty = 2.0$). The results demonstrate that as the wall temperature increases, the drag coefficient, the rms values of the lift coefficients and the mean separation angle decrease, while the recirculation length and the pressure coefficient at the rear stagnation point increase. The vortex shedding frequency remains unchanged for the three isothermal wall conditions. The influences from the wall temperature are concentrated mainly in the near-wall layer, especially before the mean separation point. The patterns for the flow, temperature, and density fields are hardly affected by the wall temperature in regions far away from the cylinder surface.

It shall be mentioned that the flow patterns and the behaviors of the integral quantities may become anomalous and interesting when the free-stream Mach number is around the upper transonic limit as observed from the experimental data. The inflow Reynolds number may also have significant effect on the flow pattern and shock wave

dynamics. These issues are not listed in the content of the present paper and are worth further research.

Acknowledgments

References

[1] A. Uranga, Assessment of Turbulence Modeling for Compressible Flow Around Stationary and Oscillating Cylinders, Masters thesis, University of Victoria, 2004.

[2] H. Bénard, Formation de centres de giration à l'arrière d'un obstacle en mouvement, Comptes Rendus de I'Academie des Sciences, 147(1908), 839-842.

[3] T. von Kármán and H. Rubach, On the mechanism of resistance of fluids and air, Physikalische Zeitschrift, 13(1912), 49-59.

[4] A. Thom, The flow past circular cylinders at low speeds, Proceedings of the Royal Society (London): A, 141(1933), 651-666.

[5] E. Berger and R. Wille, Periodic flow phenomena, Annu. Rev. Fluid Mech., 4(1972), 313.

[6] C. Norberg, Effects of Reynolds number and a low-intensity free-stream turbulence on the flow around a circular cylinder, Publication No. 87/2, Department of Applied Thermodynamics and Fluid Mechanics, Chalmers University of Technology, Sweden, 1987.

[7] P. Beaudan and P. Moin, Numerical experiments on the flow past a circular cylinder at subcritical Reynolds number, Report No. TF-62, Department of Mechanical Engineering, Stanford University, 1994.

[8] C. H. K. Williamson, Vortex dynamics in the cylinder wake, Annu. Rev. Fluid Mech., 28(1996), 477.

[9] M. M. Zdravkovich, Flow Around Circular Cylinders Volume 1: Fundamentals, Oxford University Press, 1997.

[10] M. M. Zdravkovich, Flow Around Circular Cylinders Volume 2: Applications, Oxford University Press, 2002.

[11] M. Breuer, Large eddy simulation of the subcritical flow past a circular cylinder Numerical and modeling aspects, Int. J. Numer. Meth. Fluids, 28(1998), 1281-1302.

[12] A. Travin, M. Shur, M. Strelets and P. R. Spalart, Detached-Eddy Simulations Past a Circular Cylinder, Flow, Turb. & Comb., 63(1999), 293-313.

[13] M. Breuer, A challenging test case for large eddy simulation: high Reynolds number circular cylinder flow, Int. J. Heat Fluid Flow, 21(2000), 648-654.

[14] A. G. Kravchenko and P. Moin, Numerical studies of flow over a circular cylinder at $Re_D =$ 3900, Phys. Fluids, 12(2000), 403-417.

[15] M. Strelets, Detached-eddy simulation of massively separated flows, AIAA Paper, (2001), AIAA-2001-0879.

[16] A. Travin, M. Shur, M. Strelets and P. R. Spalart, Physical and numerical upgrades in the Detached-Eddy Simulations of complex turbulent flows, in Advances in LES of Complex Flows, edited by R. Friederich and W. Rodi (Kluwer, Dordrecht), 65(2002), 239-254.

[17] P. R. Spalart, S. Deck, M. Shur, K. Squires, M. Strelets and A. Travin, A new version of detached-eddy simulation, resistant to ambiguous grid densities, Theor. Comput. Fluid Dyn., 20(2006), 181-195.

[18] S. Wornom, H. Ouvrard, M. V. Salvetti, B. Koobus, and A. Dervieux, Variational multiscale large-eddy simulations of the flow past a circular cylinder: Reynolds number effects, Computers & Fluids, 47(2011), 44-50.

[19] S. Mittal, Finite element computation of unsteady viscous compressible flows, Comput. Methods Appl. Mech. Engrg., 157(1998), 151-175.

[20] A. Burbeau and P. Sagaut, Simulation of a viscous compressible flow past a circular cylinder with high-order discontinuous Galerkin methods, Computers & Fluids, 31(2002), 867-889.

[21] C. Y. Xu, L. W. Chen, and X. Y. Lu, Large-eddy simulation of the compressible flow past a wavy cylinder, J. Fluid Mech., 665(2010), 238-273.

[22] J. M. Macha, Drag of Circular Cylinders at Transonic Mach Numbers, AIAA J., 14(1977) 605-607.

[23] V. S. Murthy and W. C. Rose, Detailed Measurements on a Circular Cylinder in Cross Flow, AIAA J., 16(1978),549-550.

[24] O. Rodriguez, The Circular Cylinder in Subsonic and Transonic Flow. AIAA J., 22(1984), 1713-1718.

[25] R. F. B. Miserda and R. G. Leal, Numerical Simulation of the Unsteady Aerodynamic Forces over a Circular Cylinder in Transonic Flow, AIAA paper, AIAA-2006-1408, 2006.

[26] C. Y. Xu, L. W. Chen, and X. Y. Lu, Effect of Mach number on transonic flow past a circular cylinder, Chinese Sci. Bull., 54(2009), 1886-1893.

[27] N. V. Nikitin, F. Nicoud, B. Wasistho, K. D. Squires and P. R. Spalart, An approach to wall modeling in large-eddy simulations, Phys. Fluids, 12(2000), 1629-1632.

[28] J. Fröhlich and D. von Terzi, Hybrid LES/RANS methods for the simulation of turbulent flows, Prog. Aerosp. Sci., 44(2008), 349-377.

[29] P. R. Spalart, Detached-eddy simulation, Annu. Rev. Fluid Mech., 41(2009), 181-202.

[30] S. Y. Chen, Z. H. Xia, S. Y. Pei, J. C. Wang, Y. T. Yang, Z. L. Xiao and Y. P. Shi, Reynolds-stressed-constrained large eddy simulation of wall bounded turbulent flows, J. Fluid. Mech., 703(2012), 1-28.

[31] Z. Jiang, Z. L. Xiao, Y. P. Shi and S. Y. Chen, Constrained large eddy simulation of wall-bounded compressible turbulent flows, Submitted to Phys. Fluids, 2013.

[32] S. Y. Chen, Y. C. Chen, Z. H. Xia, K. Qu, Y. P. Shi, Z. L. Xiao, Q. H. Liu, Q. D. Cai, F. Liu, C. B. Lee, R. K. Zhang, and J. S. Cai, Constrained Large-Eddy Simulation and Detached Eddy Simulation of Flow Past a Commercial Aircraft at 14 Degrees Angle of Attack, Sci. China, Phys. Mech. Astron., 56(2013), 270-276.

[33] A. Favre, Turbulence: space-time statistical properties and behavior in supersonic flows, Phys. Fluids A, 23(1983), 2851.

[34] D. Knight, G. Zhou, N. Okong'o, and V. Shukla, Compressible large eddy simulaton using unstructured grids, AIAA Paper, (1998), AIAA-1998-0535.

[35] M. P. Martín, U. Piomelli and G. V. Candler, Subgrid-scale models for compressible large-eddy simulations, Theor. Comput. Fluid Dyna., 13(2000), 361-376.

[36] P. R. Spalart, W. H. Jou, M. Strelets, and S. R. Allmaras, Comments on the feasibility of LES for wings, and on a hybrid RANS/LES approach, in Advances in DNS/LES, Proceedings of 1st AFOSR International Conference on DNS/LES, Ruston, LA, edited by C. Liu and Z. Liu (Greyden Press, Columbus, OH), (1997), 137-147.

[37] P. R. Spalart and S. R. Allmaras, A one-equation turbulence model for aerodynamic flows, Recherche Aerospatiale No. 1(1994), 5-21.

[38] J. R. Edwards and S. Chandra, Comparison of eddy viscosity-transport turbulence models for three-dimensional, shock-separated flowfields, AIAA J. 34(1996), 756-763.

[39] K. D. Squires, Dynamic subgrid scale modeling of compressible turbulence, Annu. Res. Brief, Stanford Uni., (1991), 207-223.

[40] C. Brun, M. P. Boiarciuc, M. Haberkorn, and P. Comte, Large eddy simulation of compressible channel flow: Arguments in favour of universality of compressible turbulent wall bounded flows, Theoret. Comput. Fluid Dyn., 22(2008), 189-212.

[41] K. Sengupta, G. B. Jacobs, and F. Mashayek, Large-eddy simulation of compressible flows using a spectral multidomain method, Int. J. Numer. Methods Fluids, 61(2009), 311-340.

[42] M. S. Liou and J. C. J. Steffen, A new flux splitting scheme, J. Comput. Phys., 107(1993), 23-39.

[43] M. S. Liou, A sequel to AUSM: AUSM+, J. Comput. Phys., 129(1996), 364-382.

[44] M. S. Liou, Mass flux schemes and connection to shock instability, J. Comput. Phys., 160(2000), 623-648.

[45] B. van Leer, Towards the ultimate conservative difference scheme V. A second order sequel to Godunovs method, J. Comput. Phys., 32(1979), 101.

[46] H. Oertel and J. Affiliation, Wakes behind blunt bodies, Annu. Rev. Fluid Mech., 22(1990), 539-564.

[47] J. C. Owen and P.W. Bearman, Passive control of viv with drag reduction, J. Fluids Struct., 15(2001), 597-605.

[48] H. G. Pagendarm, B. Seitz, and S. I. Choudhry, Visualization of shock waves in hypersonic CFD solutions, Tech. Rep., DLR, 1996.

[49] B. Verman, H. Kuerten, and B. Geurts, Shocks in direct numerical simulation of the confined three-dimensioal mixing layer, Phys. Fluids, 7(1995), 2105-2107.

[50] J. B. Freund, S. K. Lele, and P. Moin, Compressibility effects in a turbulent annular mixing layer. Part 1. Turbulence and growth rate, J. Fluid Mech., 421(2000), 229-267.

[51] L. H. Jorgensen, Prediction of static aerodynamic charateristics for space shuttle like and other bodies at angles of attack from 0 to 180, Tech. Rep., NASA, TN-D-6996, 1973.

[52] C. J. Welsh, The drag of finite length cylinders determined from flight tests at high reynolds numbers for a mach number range from 0.5 to 1.3, Tech. Rep., NACA, TN-2941, 1953.

[53] J. M. Macha, A wind tunnel investigation of circular and straked cylinders in transonic cross flow, Tech. Rep., Texas A/M Research Foundation, College Station, Texas, TAMU-Rept.-3319-76-01, 1976.

[54] A. B. Wang, Z. Trávnícek, and K. C. Chia, On the relationship of effective Reynolds number and Strouhal number for the laminar vortex shedding of a heated circular cylinder, Phys. Fluids, 12(2000), 1041.

[55] M. Sabanca and F. Durst, Flows past a tiny circular cylinder at high temperature ratios and slight compressible effects on the vortex shedding, Phys. Fluids, 15(2003), 1821.